AGU PUBLICATIONS

Geochemistry, Geophysics, Geosystems

Linking basin-scale and pore-scale gas hydrate distribution patterns in diffusion-dominated marine hydrate systems

Michael Nole[1] , **Hugh Daigle**[1] , **Ann E. Cook**[2] , **Jess I. T. Hillman**[2,3], and **Alberto Malinverno**[4]

[1]Department of Petroleum and Geosystems Engineering, University of Texas at Austin, Austin, Texas, USA, [2]School of Earth Sciences, Ohio State University, Columbus, Ohio, USA, [3]GEOMAR Helmholtz Centre for Ocean Research, Kiel, Germany, [4]Lamont Doherty Earth Observatory of Columbia University, Palisades, New York, USA

Key Points:
- We show potential distribution patterns of methane hydrate that can preferentially accumulate in coarse-grained sands via diffusion
- One-dimensional simulations demonstrate the impact of pore size distributions and sand layer thickness on gas hydrate distributions within sand layers
- In 2-D and 3-D, concentration gradients in multiple dimensions and competition between sand layers can limit methane transport

Correspondence to:
M. Nole,
michael.nole@utexas.edu

Abstract The goal of this study is to computationally determine the potential distribution patterns of diffusion-driven methane hydrate accumulations in coarse-grained marine sediments. Diffusion of dissolved methane in marine gas hydrate systems has been proposed as a potential transport mechanism through which large concentrations of hydrate can preferentially accumulate in coarse-grained sediments over geologic time. Using one-dimensional compositional reservoir simulations, we examine hydrate distribution patterns at the scale of individual sand layers (1–20 m thick) that are deposited between microbially active fine-grained material buried through the gas hydrate stability zone (GHSZ). We then extrapolate to two-dimensional and basin-scale three-dimensional simulations, where we model dipping sands and multilayered systems. We find that properties of a sand layer including pore size distribution, layer thickness, dip, and proximity to other layers in multilayered systems all exert control on diffusive methane fluxes toward and within a sand, which in turn impact the distribution of hydrate throughout a sand unit. In all of these simulations, we incorporate data on physical properties and sand layer geometries from the Terrebonne Basin gas hydrate system in the Gulf of Mexico. We demonstrate that diffusion can generate high hydrate saturations (upward of 90%) at the edges of thin sands at shallow depths within the GHSZ, but that it is ineffective at producing high hydrate saturations throughout thick (greater than 10 m) sands buried deep within the GHSZ. Furthermore, we find that hydrate in fine-grained material can preserve high hydrate saturations in nearby thin sands with burial.

Plain Language Summary This study combines one-, two-, and three-dimensional simulations to explore one potential process by which methane dissolved in water beneath the seafloor can be converted into solid methane hydrate. This work specifically examines one end-member methane transport mechanism, diffusion, and its potential to help grow methane hydrate in the pore space of marine sediments. The simulations presented here span hundreds of thousands of years to capture the evolution of a diffusion-dominated gas hydrate system over geologic time.

1. Introduction

Gas hydrates are ice-like compounds composed of low molecular weight gases trapped in water lattices that are stable at high pressure and low temperature [*Sloan and Koh*, 2007]. Naturally occurring hydrates typically contain methane as the guest molecule, so accumulations of hydrate worldwide constitute unconventional reservoirs of natural gas. Natural methane hydrates can form within the sediments of any subsurface environment globally where the appropriate thermodynamic conditions for stability are met and enough dissolved gas is available to come out of solution and precipitate as a solid [*Kvenvolden*, 1998; *Buffett*, 2000]. These conditions most commonly exist along marine continental margin environments as well as under arctic permafrost [*Paull and Dillon*, 2001]. Methane hydrate deposits are increasingly of interest worldwide for their resource potential [*Collett*, 2002] as well as their ability to impact global climate change [*Dickens et al.*, 1995] and submarine slope stability [*Mienert et al.*, 2005].

In the Gulf of Mexico, salt-withdrawal basins of the outer continental shelf have been the subject of much attention in recent years due to their abundance of naturally occurring methane hydrate deposits. Methane hydrate accumulations in the area have historically been investigated for their potential as a drilling hazard [*Milkov et al.*, 2000]; more recently, they have come to be viewed as a potential energy

resource [*Boswell et al.*, 2012; *Frye*, 2008]. A location in Walker Ridge Block 313 (WR313) in the Terrebonne Basin is an interesting site with a variety of hydrate reservoirs and hydrate morphology. Logging-while-drilling (LWD) data collected at the Terrebonne Basin by the Chevron-DOE Joint Industry Project (JIP) indicated high hydrate saturation occupying the pore space of both thick sand reservoirs (10–25 m scale) and thin isolated sand layers (∼3 m or less). Fracture-hosted hydrate in fine-grained sediments was also identified, with one such unit over 100 m thick [*Frye et al.*, 2012]. In addition to the LWD data from two wells, 2-D and 3-D seismic data has been acquired in the Terrebonne Basin [*Frye et al.*, 2012; *Haines et al.*, 2014].

Interpretations of well log and seismic data in this region provide different hypotheses for the dominant methane migrations mechanisms at play to produce observed saturations of methane hydrate. Advective, updip methane flux through sandy strata from a deep methane source has been proposed as a potential transport mechanism for thick, deep hydrate deposits (near the BHSZ) in the region, as regional seismic interpretation indicates the presence of a free gas phase beneath the BHSZ [*Boswell et al.*, 2012; *Frye et al.*, 2012]. Since hydrate forms in pore space and reduces sediment permeability, high hydrate saturations in thin sands have also been implicated in overpressure generation and fracturing in advective systems; one-dimensional (1-D) models have been developed to explain such occurrences and the time scales over which they can develop [*Daigle and Dugan*, 2010; *Daigle and Dugan*, 2011]. Furthermore, flow focusing as an advective fluid transport mechanism in overpressured marine systems can enhance methane transport in the presence of clay-sand effective methane solubility contrasts [*Nole et al.*, 2016]. These mechanisms can charge thick or thin sands alike, while high hydrate saturations generated by a diffusive transport mechanism tend to be found mainly in thin sands.

Well log data and 1-D modeling of sands at WR313 have been used to suggest a dominantly diffusive migration mechanism in shallow, thin sands from microbially produced methane in clayey strata adjacent to a 2.5 m thick sand layer [*Cook and Malinverno*, 2013]. High hydrate saturations in the pores of thin, sandy layers [*Frye et al.*, 2012] are also observed in some locations to occur between fracture-hosted hydrates in bounding clays [*Cook et al.*, 2008]. The presence of hydrate-free zones separating hydrate in clays from hydrate in sands has been suggested as evidence that diffusion along clay-sand spatial solubility discontinuities can act as a dominant transport mechanism to supply methane to thin, shallow sands [*Malinverno*, 2010; *Cook and Malinverno*, 2013; *Malinverno and Goldberg*, 2015].

At the reservoir scale, gas hydrate systems modeling solves coupled systems of mass and energy conservation equations to explain observations unique to different hydrate-bearing environments. One-dimensional modeling has been performed to describe gas hydrate accumulations in marine sediments under varying fluid flux conditions, methanogenesis rates, and sedimentation rates [*Davie and Buffett*, 2001, 2003; *Bhatnagar et al.*, 2007; *Garg et al.*, 2008]. This methodology has been expanded into 2-D, where effects of permeability anisotropy, gas buildup beneath the base of the hydrate stability zone (BHSZ), and sediment fracturing on methane hydrate accumulations in porous media have been compared to 1-D simulation results and well log interpretations [*Chatterjee et al.*, 2014]. These studies have provided useful benchmarks for better understanding dynamic hydrate systems. We build upon their methods by incorporating pore size distribution effects on methane solubility, employing a Lagrangian reference frame in 1-D and 2-D with a rhombic grid system for 2-D simulations, and performing 3-D simulations with time-varying grid properties with a modeled basin stratigraphy informed by interpreted seismic data.

The goal of this study is to computationally determine potential gas hydrate distribution patterns in coarse-grained sand layers where diffusion is the dominant methane transport mechanism. We simulate diffusion-dominated gas hydrate systems in one, two, and three dimensions similar to that of the Terrebonne Basin in the Gulf of Mexico. In our models, we consider a range of sand thicknesses varying from 3 m (similar to the thin sand described by *Cook and Malinverno* [2013]), which we refer to as the Red Sand, to 10.5 and 25 m, which we call the Orange and Blue Sands respectively and are similar to those encountered in the Terrebonne Basin [*Frye et al.*, 2012]. We employ 1-D and 2-D simulations in a moving reference frame to understand local hydrate accumulations within and immediately surrounding a thin sand layer. We then expand to a 3-D reservoir model to assess hydrate distribution patterns on a regional scale between multiple dipping sand bodies. We show that at a local scale, capillary inhibition with hydrate growth can progress from the outer boundary toward the center of a sand body [*Rempel*, 2011], causing a smoothing effect on hydrate saturation distributions throughout the

sand. On a regional scale, we show that the geometry of sand layers as well as the spatial relationship between multiple dipping sands can dramatically influence gas hydrate distribution patterns.

2. Methods

Simulations performed in this study build upon the methane hydrate reservoir simulator developed by *Sun and Mohanty* [2006]. The simulator uses a fully implicit, finite volume difference scheme with primary variable switching to solve a coupled system of mass balance equations for water and methane along with a system energy balance. The simulator is stable on large length scales and over geologic timespans. Hydrate formation and dissolution are tracked by assuming local equilibrium corresponding to the thermodynamic state of each grid block. If a grid block contains dissolved methane in concentrations exceeding the aqueous-phase solubility at a given pressure and temperature, excess methane partitions into the hydrate and/or gas phase. The model domains employed in this work are situated entirely within the gas hydrate stability zone (GHSZ), so methane in excess of aqueous solubility only forms hydrate.

We made several modifications to the simulation methodology for the work presented here. The pore water in shallow marine sediments is saline, and the addition of a salt component alters the equilibrium solubility conditions of methane in pore water. Hydrate forms in confined sediment pore space, which alters the Gibbs free energy of the pore system in comparison to a bulk system and results in a phenomenon known as the Gibbs-Thomson effect [*Clennell et al.*, 1999]. An increase in effective methane solubility due to the Gibbs-Thomson effect is significant in the small pores of fine-grained, clay-rich sediments. Pore space in sediments is characterized by a distribution of pore sizes, so the increase in solubility due to the Gibbs-Thomson effect should become more significant as gas hydrate saturation increases, filling progressively smaller pores [*Liu and Flemings*, 2011]. In marine environments, methanogens beneath the seafloor work to convert buried organic matter to methane, constituting a major source of methane in hydrate-bearing sediments in addition to methane produced by thermogenic processes. Organic matter is mostly preserved in fine-grained sediments [*Hedges and Keil*, 1995], and methanogenesis is active in clay-rich units [*Claypool and Kaplan*, 1974]. Furthermore, the simulated system is not static; sedimentation consistently pushes sediment layers downward relative to the seafloor, increasing temperature and pressure, which in turn affect hydrate formation and dissolution. Throughout this process, compaction of pore space reduces porosity, resulting in upward fluid motion with respect to solid sediment grains [*Berner*, 1980].

2.1. Salt Mass Balance in Pore Water

Our methane hydrate reservoir simulator makes use of an empirical three-phase equilibrium pressure-temperature (P-T) correlation for Structure I methane hydrate in a bulk system of pure water [*Moridis*, 2003]. In marine hydrate-bearing environments, the P-T curve is affected by the presence of dissolved salt in pore fluid, which inhibits hydrate formation [*Koh et al.*, 2002].

For the purposes of marine sediment simulations, the P-T curve can be translated by a temperature increment ΔT^{hyd} if salt is present in the pore water, given by the following equation [*Sloan and Koh*, 2007]:

$$\frac{\Delta T^{hyd}}{T_w(T_w - \Delta T^{hyd})} = 0.6652 \frac{\Delta T^{fus}}{T_f(T_f - \Delta T^{fus})}, \tag{1}$$

where T_w is the freezing temperature of hydrate in a salt-free system, ΔT^{fus} is the hydrate freezing temperature depression at atmospheric pressure for a given salt mass fraction, and T_f is the freezing temperature of water. The hydrate freezing temperature depression at atmospheric conditions is calculated from data tabulation as follows [*Haynes and Lide*, 2010]:

$$\Delta T^{fus} = w_A^s\left(164.49 w_A^s + 49.462\right), \tag{2}$$

where w_A^s is the mass fraction of salt in the aqueous phase, in kg salt/kg fluid. The P-T diagram is thus translated as follows:

$$T = T_0 + \Delta T^{hyd}, \tag{3}$$

where T_0 is the in situ pore water temperature, and T is the temperature in pure water whose equilibrium pressure would correspond to the equilibrium pressure of a saline system at T_0. In the presence of dissolved

salt, hydrate precipitates at a lower temperature for a given pressure (or at a higher P for a given T) compared to pure water.

Additionally, when methane hydrate forms in pore space, pure water and methane are the only two constituents of the hydrate phase. Salt in the pore water is therefore excluded from the hydrate phase, and because water is consumed upon formation of hydrate, the pore water salt concentration increases. This leads to a situation whereby hydrate formation locally increases pore water salt concentration, which in turn increases methane solubility in the pore water, inhibiting the formation of methane hydrate until the excess salt diffuses out or less saline water flows in.

2.2. The Gibbs-Thomson Effect

Methane hydrate formation occurs when the concentration of methane dissolved in pore water exceeds its solubility at a specified pressure, temperature, and pore water salinity. Additionally, decreasing the size of a pore increases the surface area to volume ratio of the pore space, and hydrate crystals that nucleate in these pores must have correspondingly large surface area to volume ratios. In fine-grained sediments, the increase in curvature of the interface between a nucleating mass of hydrate and surrounding pore water is significant enough that the contribution of interfacial energy to the total Gibbs free energy of the pore water-methane system cannot be neglected. This in turn leads to an increase in the solubility of methane in the pore space, inhibiting hydrate growth [*Clennell et al.*, 1999].

An increase in methane solubility with decreasing pore radius corresponds to a decrease in the equilibrium triple point temperature of methane in the pore space, known as the Gibbs-Thomson effect. Thus, methane hydrate requires lower temperatures for nucleation in smaller pores than in larger pores, all else being equal. This phenomenon is implemented in the simulator as a translation of the phase diagram dependent on the effective pore radius of the grid block of interest. The change in methane hydrate freezing temperature is calculated as follows [*Anderson et al.*, 2009]:

$$\Delta T_m = \frac{-2 T_{mb} \sigma_{hl} \cos(\theta)}{H_f \rho_h r_e}, \tag{4}$$

where T_{mb} is the freezing temperature of methane hydrate in bulk water, σ_{hl} is the solid-liquid interfacial energy between hydrate and water, θ is the hydrate wetting angle to the pore surface, H_f is the hydrate bulk enthalpy of fusion, ρ_h is the density of methane hydrate, and r_e is the effective pore radius describing the change in freezing temperature in a pore of radius r_e.

For a given in situ temperature T_0 within the pore space, the temperature is therefore adjusted when calculating the hydrate freezing pressure as follows before being used to calculate the corresponding three-phase equilibrium pressure:

$$T = T_0 \left(1 + \frac{2 \sigma_{hl} \cos(\theta)}{H_f \rho_h r_e}\right). \tag{5}$$

2.3. Steady State Methanogenesis

In the shallow subsurface of marine methane hydrate-bearing environments beneath the sulfate reduction zone, microbes known as methanogens convert organic material that has been deposited on the seafloor into methane [*Claypool and Kaplan*, 1974]. Methanogens typically act in organic-rich, clayey sediments and are inactive in sandy units [*Waseda*, 1998; *Pohlman et al.*, 2009]. Because the average pore size in clays is smaller than that in sandy layers, the solubility of methane in fine-grained layers is higher than the solubility of methane in the sands. Also, as the organic matter in the clayey layers is consumed by methanogens, less organic matter remains and therefore less methane is produced as burial proceeds.

A dynamic system therefore typically exists with respect to methanogenesis in marine gas hydrate systems. At steady state, the microbial methane production rate can be expressed as a decreasing function of depth as organic matter is consumed. Methanogenesis only takes place in the presence of organic matter, which is often associated with fine-grained sediments, and since these sediments can hold more aqueous methane in solution than the coarse-grained sand layers due to their small pore sizes, aqueous methane concentration gradients typically exist between clayey and sandy layers [*Malinverno*, 2010]. This drives a diffusive flux from fine-grained clays to coarse-grained sands, promoting hydrate growth in the coarse-grained layers

due to short diffusive migration of methane, or diffusive methane transport between adjacent layers within the GHSZ.

Steady state methane generation due to microbial methanogenesis is implemented following the formulation of *Malinverno* [2010] as follows:

$$q(z) = k_\alpha \lambda \alpha_{SMT} e^{-\frac{\lambda}{\omega}(z - z_{SMT})}, \tag{6}$$

where $q(z)$ is a 1-D depth-varying source of methane into the pore space, k_α is a conversion factor from metabolizable organic carbon mass fraction to dissolved methane concentration, λ is the reaction rate of microbial methanogenesis, α_{SMT} is the mass fraction of metabolizable organic carbon at the sulfate-methane transition (SMT), ω is the sedimentation rate, and z_{SMT} is the depth below seafloor of the SMT. To justify a steady state methanogenesis assumption, the domain simply assumes that methanogens are already present in clayey strata throughout the sediment column as an initial condition. This depth-varying methane source term is imposed only upon grid blocks specified as clay and not sand.

2.4. Sedimentation

Over geologic time, sedimentation works not only to consolidate sediments, as has commonly been investigated with marine hydrate simulations, but it also brings in sediments with heterogeneous physical properties as sediment sources and depositional environments change. Because lithology can exert an important control on permeability, porosity, and pore size distribution in the subsurface, our simulations incorporate lithologic heterogeneity by formulating all relevant grid properties as functions of time and space.

For the environments simulated here, a binary system of sand and clay strata was considered, although in reality geologic systems are certainly more complicated. To identify the sand units in the stratigraphic column in the Terrebonne Basin, logging-while drilling well log data was analyzed from two JIP Leg 2 wells [*Collett et al.*, 2012]. Then, to extend the stratigraphic interpretation over the basin, the well logs were tied to 3-D seismic data by developing synthetic seismograms for each well. Information describing the Red, Blue, Orange, and Green sands [*Frye et al.*, 2012] was then fed into the 3-D simulator as latitude, longitude, and depth coordinates corresponding to the mapped top and bottom surfaces of the sand layers. All grid blocks outside of the sand horizons are considered to be clay. Different lithologies can easily be incorporated using this method by simply making the grid block designations dependent on the specific imported horizon.

Once the sand layers are loaded into the grid, the 3-D simulations use a sedimentation velocity and simulation end time to determine the depth at present time that would correspond to the seafloor depth at the beginning of the simulation. The position and orientation of each sand layer as a function of time are interpolated between the initial sand layer geometries at deposition and their current observed geometries. In the simulations presented in this study, sand layers are deposited originally as horizontal beds whose dip and depth increase with burial. Although a constant sedimentation velocity characterizes each grid block, the sedimentation velocity can vary laterally, resulting in an evolving dip of the sand layers. The solid hydrate phase is carried downward with sedimentation. While this is a simplification of depositional history and does not capture more dynamic geologic processes pertaining to uplift and deformation, it is sufficient for our purposes to capture first-order effects of sand layer burial and rotation on hydrate accumulation patterns.

2.5. Grid Formulations, Boundary Conditions, and Initial Conditions

One- and two-dimensional simulations were performed on a small scale to assess the impact of methane diffusion on gas hydrate distributions within and immediately surrounding a thin sand layer as it is buried through the GHSZ. In these simulations, we adopt a Lagrangian reference frame: boundary conditions change through time in the simulation to reflect increasing pressure and temperature with burial. The system pressure is adjusted by adding hydrostatic pressure throughout the domain at each time step according to the change in burial depth, and the temperature is correspondingly adjusted by increasing temperature according to the geothermal gradient. The methane concentrations at the boundaries of the domain, away from the sand layer, are set to the steady state solution without a sand layer present (the steady state solution is time-invariant and does not need to be solved at each time step). Methane concentrations change as a result of changing methanogenesis rates, which are also adjusted throughout the
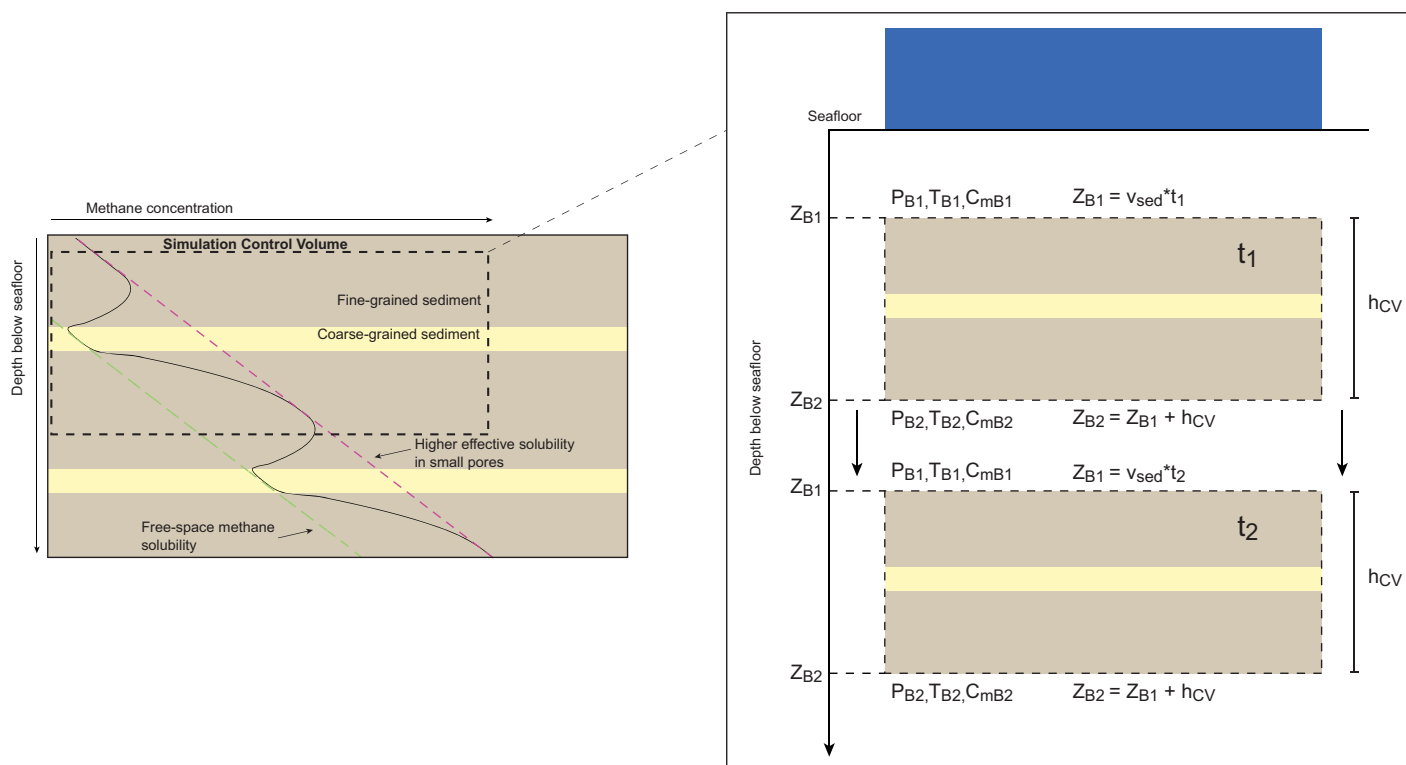
Figure 1. (left) A fully developed methane concentration profile in a repeating sequence of alternating fine- and coarse-grained sediments with the free space methane solubility (dashed green line) and clay layer methane solubility (dashed magenta line) superimposed. (right) The control volume in 1-D centers around a sand layer that is buried over time. Boundary conditions change with time.

domain at each time step. The time step is variable and changes according to rate of solution convergence, with a minimum time step of approximately 200 days. Three-dimensional simulations were performed in an Eulerian reference frame with static boundary conditions; as coarse-grained sand layers are buried through the domain, new fine-grained material is deposited on top.

The 1-D simulation control volume is depicted in Figure 1. In these simulations, a compaction-driven flux boundary condition varies with time at the bottom of the domain. Compaction moves fluid upward relative to the sediment grains and diminishes as the change in porosity of the system with burial approaches zero. This stands in contrast to a fixed reference frame (as in the 3-D simulations performed here), in which compaction-driven fluid flow is downward when the reference frame is fixed at the seafloor [e.g., *Bhatnagar et al.*, 2007; *Frederick and Buffett*, 2011]. The top of the domain is kept at a constant pressure corresponding to hydrostatic pressure at the depth of the boundary. While this pressure may not be exactly hydrostatic (if fluid is moving upward above the domain), the magnitude of any overpressure in this control volume due to compaction flux has a negligible impact on methane solubility throughout the domain. Boundary temperatures are fixed along a geothermal gradient. The simulation boundaries are placed sufficiently far from the sand such that hydrate growth in the sand is separated from hydrate in clays by hydrate-free zones. Initially, methane is absent from the system at the SMT, and the methane concentrations on the top and bottom boundaries are set equal to the methane concentrations in their respective adjacent grid blocks with the addition of dissolved methane due to methanogenesis on the boundaries. All grid blocks in 1-D are 0.6 m thick. The thickness of the entire sand layer varies from 1.8 to 18 m with 25.5 m of clay both above and below the sand layer, for a total domain length of between 52.8 and 69 m.

In 2-D, the simulation domain is discretized into an array of right rhombic prisms; the gravity vector is rotated to simulate a dipping sand (Figure 2a). This is important because in a rectangular grid system oriented orthogonal to gravity, the edge of a dipping sand must be described by a discrete step function, across which diffusion can act laterally and vertically. When the scale of grid discretization is on a similar order of magnitude to the thickness of the sand itself, a jagged sand edge could yield unwanted methane diffusion
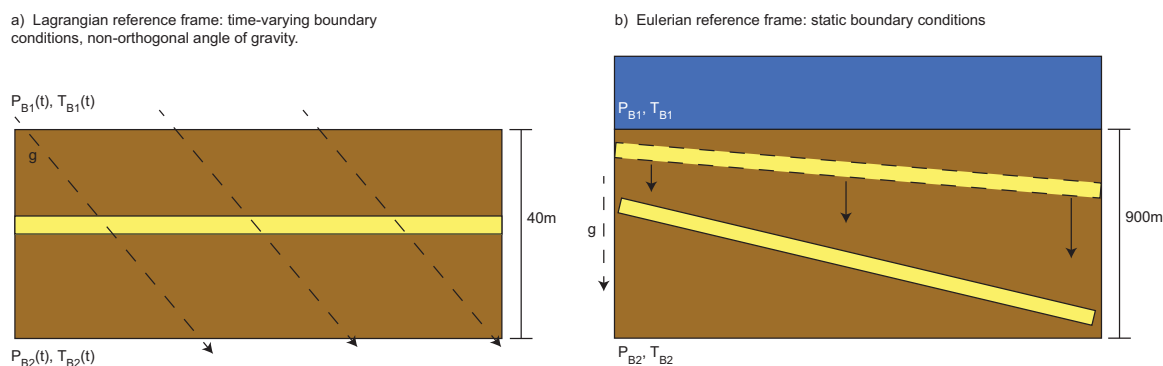
a) Lagrangian reference frame: time-varying boundary conditions, non-orthogonal angle of gravity.

b) Eulerian reference frame: static boundary conditions

Figure 2. (a) A moving (Lagrangian) reference frame is used for 1-D and 2-D simulations of hydrate distributions within and around single sand layers. Dashed lines represent the gravity vector, which rotates to simulate the dip of the sand in 2-D. (b) A static (Eulerian) reference frame is implemented in this study for 3-D basin-scale simulations.

parallel to the sand surface. Boundary conditions are formulated in the same way as described for 1-D simulations. Also as in 1-D, the system is initially devoid of methane, so the hydrate formation and dissolution patterns reflect the maximum amount of hydrate dissolution possible for a given set of methanogenesis parameters. On the top and bottom boundaries, methane concentrations are formulated as functions of time in the same way as in 1-D simulations: at each time step, the methane concentration on each boundary is set to the methane concentration in the grid block adjacent to the boundary at the previous time step plus the addition of methane due to methanogenesis on the boundary. On the sides of the domain, no flux boundary conditions are prescribed for methane concentrations. The simulated sand layer is discretized as one 3.6 m grid block. The downdip length of the sand layer in these simulations is set at 100 m, discretized into 20 grid blocks. Though compaction-driven flow can focus in the high-permeability sand layer in the 2-D simulations, discussion of flow focusing is beyond the scope of this work.

In 3-D, a static system in an Eulerian reference frame buries sand layers through a fixed domain (Figure 2b). The top boundary is set at seafloor hydrostatic pressure, the bottom boundary condition is that of constant advective compaction flux, and constant temperature boundary conditions on the top and bottom of the domain are defined by the geothermal gradient. As initial conditions, methane concentrations and methane hydrate saturations throughout the domain are set to zero; therefore, the results of these simulations yield maximum dissolution rates for a given set of environmental parameters. The 3-D grid is comprised of 11,250 grid blocks (50 in the downward z direction and 15 in each lateral dimension), discretizing a basin system that spans 13.3 km by 9.8 km laterally and 915 m in the depth dimension. This resolution yields a sand grid block vertical thickness of 18.3 m, which is about 5 times the thickness of the individual sand unit modeled in 2-D.

One- and two-dimensional simulations are limited in that they cannot describe regional-scale gas hydrate distribution patterns; 1-D simulations illustrate hydrate distributions within a sand layer itself, while 2-D simulations demonstrate how methane solubility gradients in multiple directions affect average hydrate saturations in and around a thin sand layer. The benefit of 1-D and 2-D simulations is that they provide results at a resolution not possible in 3-D simulations due to computational limitations. Three-dimensional simulations are therefore not able to resolve hydrate-free zones immediately surrounding sand layers; nor can they depict gas hydrate distributions within individual sands. They do, however, illustrate regional gas hydrate distribution trends across multiple dipping, nonplanar sands. To ensure consistency of the numerical methods between 1-D, 2-D, and 3-D simulations, all simulations are run using a finite volume methodology. All simulations are run in 3-D; the second and third dimension are rendered trivial in 1-D simulations, and the third dimension is rendered trivial in 2-D simulations.

2.6. Incorporating Observations From Well Logs, Laboratory Measurements, and Seismic Data
2.6.1. Observations at the Terrebonne Basin
In the Terrebonne Basin, the JIP Leg 2 drilled two wells, hole WR313-G and hole WR313-H, targeting two reservoir sand units near the base of the gas hydrate stability zone: the Blue sand and the Orange sand [Boswell et al., 2012; Frye et al., 2012]. Logging-while-drilling measurements revealed that the Blue sand unit contains sandy layers interbedded with clays for a total hydrate-filled sand of ∼25 m, whereas the deeper
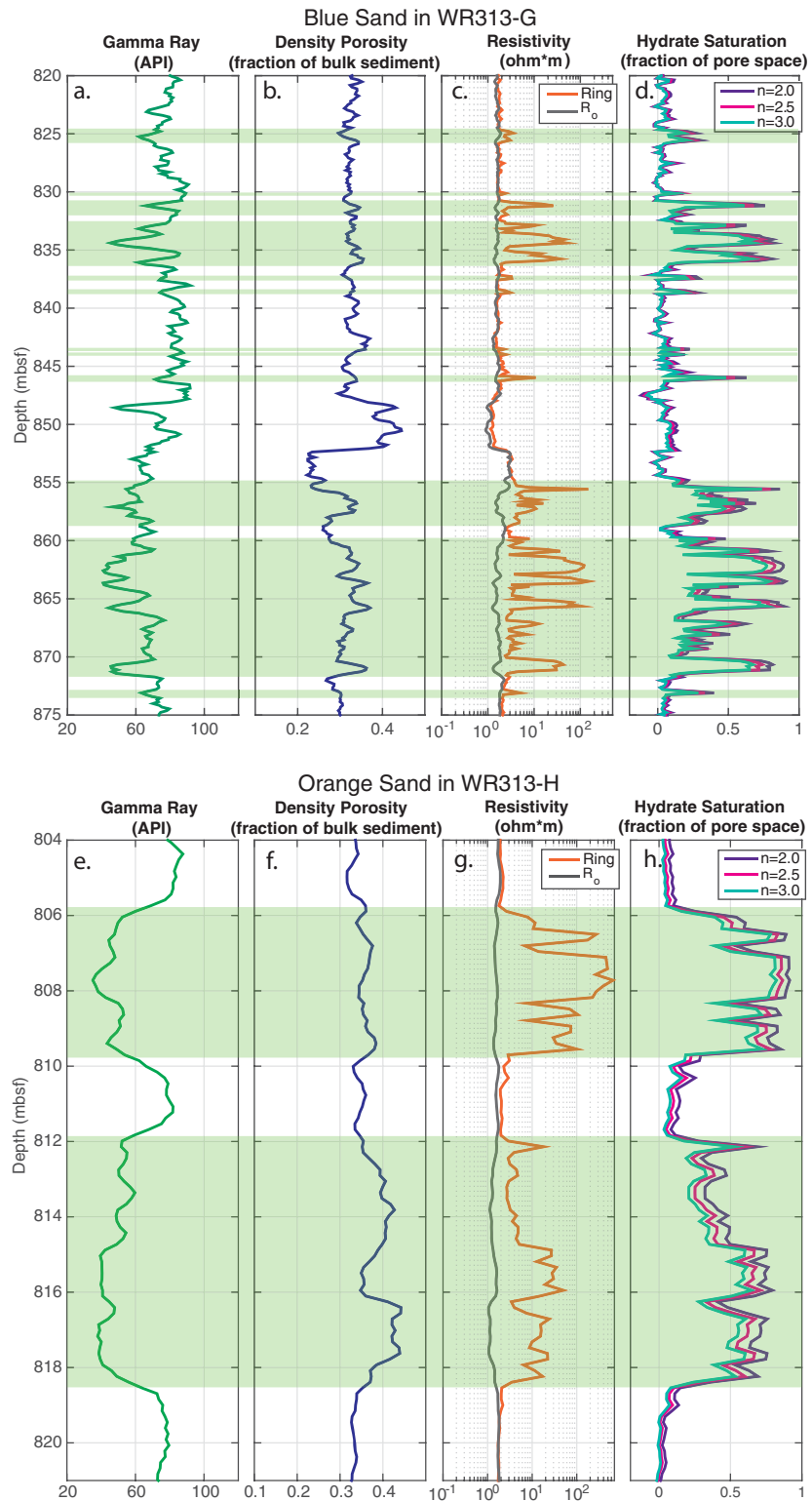
Figure 3. Measured and calculated logs from (a–d) Hole WR313-G Blue sand unit and (e–h) Hole WR313-H Orange sand unit in meters below seafloor (mbsf). Interpreted hydrate-bearing sands are highlighted in green. Figures 3a and 3e show the measured gamma ray log, which indicates sandier layers to the left (lower API) and clay-rich layers to the right (higher API). Figures 3b and 3f show the density porosity, which is corrected for the hydrate saturation. The measured ring resistivity is shown in Figures 3c and 3g along with R_0, the resistivity of the formation in the absence of hydrate. The calculated hydrate saturation is presented in Figures 3d and 3h.

Orange sand was comprised of two main lobes for a total of 10.5 m of hydrate-filled sand (Figure 3a). Thicknesses reported here are larger than by *Frye et al.* [2012] and *Boswell et al.* [2012], as they only considered high saturation ($S_h > 0.5$) gas hydrate. In our models, we are interested not just in high saturations of hydrate, but also in accumulations with lower saturation (Figure 3).

Another 9 m thick sand, the Green sand, lies below the Orange sand. The Green sand was water saturated in Hole WR313-H because it occurred below the GHSZ, but brightening of the green horizon at the BSR in seismic data suggests that it contains hydrate within GHSZ [*Frye et al.*, 2012]. A number of thin sand layers (≥ 3 m) were also identified throughout Holes WR313-G and WR313-H; some sand layers contain gas hydrate and other sand layers are water-saturated. A number of thin sand layers (≥ 3m) were also identified throughout holes WR313-G and WR313-H. Some of these sand layers contain gas hydrate and others are water saturated. One particular 2.5 m sand, called Unit A by *Boswell et al.* [2012] and *Cook and Malinverno* [2013], appears near 290 meters below seafloor (mbsf) within a 150 m thick clay-rich unit containing gas hydrate filled fractures. To maintain consistency with the sand naming scheme in the Terrebonne Basin, we refer to this 2.5 m sand as the Red sand. The Red sand has a combination of interesting characteristics: for example, the hydrate in the sand is concentrated near the top and bottom of the sand. Surrounding the sand, a hydrate-free zone persists within the bounding clays for several meters before hydrate is again observed in fractures. These features lead *Cook and Malinverno* [2013] to propose that the Red sand could be filled with hydrate as the result of diffusive methane migration from the surrounding clay, which they termed short migration.

In our 1-D models, we can use fine enough grid cells to explore hydrate accumulation patterns leading to the features observed by *Cook and Malinverno* [2013]. Because of the limitations of the grid block thickness as we increase the dimensionality of our models, however, we do not try to incorporate the fine details of these sand layers but instead use the WR313 well logs and mapped seismic horizons as a guide to the relative placement of the Red, Blue, Orange, and Green sand layers within the basin.

2.6.2. Incorporating Lithologic Heterogeneities

The simulation environment was developed to incorporate interpreted seismic horizons directly as input information to build the structure of the simulated reservoir. It then uses this data when building the structure of the grid to calculate spatial variations in sediment permeability, porosity, and pore size. Three-dimensional simulations presented here use interpreted seismic data to define sand geometries; all simulations adopt an empirical porosity-depth trend due to compaction formulated for Walker Ridge sediments from log data as follows:

$$\phi(z) = 0.35e^{-0.016z} + 0.37e^{-0.00019z}, \tag{7}$$

where ϕ is the sediment porosity and z is the depth beneath the seafloor in meters. This compaction trend is applied to both the sand and the clay lithology, although at least in the upper sediment column clays compact much more than sands. Future work could improve upon these simulations by applying different compaction trends to different lithologies, but the porosity data presented by *Daigle et al.* [2015] indicate that the difference between sand and clay porosities is significant only in the first 100 mbsf at Walker Ridge.

In a porous medium containing a distribution of pore sizes, the nonwetting gas hydrate phase will preferentially fill large pores first before filling smaller pores, a phenomenon resulting from an effective solubility increase with decreasing pore size [*Clennell et al.*, 1999; *Henry et al.*, 1999; *Liu and Flemings*, 2011]. Therefore, as the sediment pore space fills with hydrate, progressively larger amounts of dissolved methane are required to precipitate hydrate in the pore space. In the present work, this phenomenon is expressed through the Gibbs-Thomson equation by assuming that the hydrate-water interfacial curvature of precipitating hydrate is constrained by the size of the pore in which it precipitates. As the radius of a spherical pore decreases, its curvature correspondingly increases. Therefore, we assume that as pore radius decreases, interfacial curvature of the hydrate contained within a pore also increases. To incorporate the effect of changing hydrate-water interfacial curvature on methane solubility vis-à-vis a pore size distribution, we describe an effective pore radius that decreases with increasing gas hydrate saturation (equation (12)).

When simulating diffusive methane transport within a thin, coarse-grained sand, pore size distributions can have a strong impact on gas hydrate growth potential. This is because the magnitude of the solubility change of methane in water due to changes in pressure and temperature across an individual sand layer is

comparable to (or even slightly smaller than) the solubility change between the largest and smallest sediment pores.

Incorporating this phenomenon is also important from the perspective of minimizing resolution-dependent hydrate growth across lithologic discontinuities. Consider a discrete system containing sand and clay intervals defined by a single pore size. If the grid discretization is decreased to increase spatial resolution, the same methane mass flux from surrounding clay to the edge of a sand grid block will produce higher saturations of gas hydrate at the sand's edges than in a lower resolution model [*Rempel*, 2011]. This can lead to practical simulation difficulties in 1-D and inconsistencies between grids of varying resolution, whereby hydrate saturations can reach 100% of the pore space available in the sand layer, and the permeability at the sand's edge can drop to zero.

In high-resolution simulations, pore water methane solubility can instead be reformulated not only as a function of pressure, temperature, salinity, and single pore characteristics but additionally as a function of the pore size distribution within a grid block. While sands are generally considered to contain large pores with negligible influence of pore curvature effects on aqueous methane solubility, a sand layer characterized by a broad pore size distribution could potentially more uniformly distribute hydrate as compared to a sand layer described by a single pore size or a narrow pore size distribution.

Using well log and MICP data on samples recovered from JIP Leg 1 drilling in Keathley Canyon Block 151 in the Gulf of Mexico, we approximate the pore size distribution in the sand layers with a lognormal distribution that has a median pore radius r_m and standard deviation σ_r [*Bihani et al.*, 2015]; we then consider how the effective pore radius influencing three-phase equilibrium in the sand layer changes as a function of pore-filling gas hydrate saturation. First, we define a lognormal cumulative distribution function in terms of incremental (effective) pore radius, r_e, total pore volume, V_{tot}, and cumulative volume in pores smaller than r_e, V:

$$\frac{V}{V_{tot}} = 0.5 \left(1 + \mathrm{erf} \left(\frac{\ln{(r_e)} - \mu}{\sqrt{2}\sigma} \right) \right), \tag{8}$$

$$\mu = \ln \left(\frac{r_m}{\sqrt{1 + \frac{\sigma_r^2}{r_m^2}}} \right), \tag{9}$$

$$\text{and} \ \ \sigma = \sqrt{\ln \left(1 + \frac{\sigma_r^2}{r_m^2} \right)}, \tag{10}$$

where μ is the location parameter and σ is the scale parameter of the distribution.

As hydrate starts forming where the increase in effective solubility is the least, the largest pores will fill with hydrate first. This process is similar to drainage of a wetting fluid in a porous medium by a nonwetting fluid. Equation (8) therefore represents the volume fraction of pore space occupied by the wetting phase, and because precipitating a nonwetting phase fills the largest pores first, increasing volume fractions of nonwetting phases are associated with decreasing effective pore radius. Therefore, equation (8) can be conceptualized as the volume fraction of wetting phase-occupied pore space in which all pores containing the wetting phase are smaller than or equal in radius to r_e. If water, gas, ice, and hydrate can fill the pore space as nonwetting phases, equation (8) can be rewritten as follows:

$$1 - S_h - S_g - S_l = 0.5 \left(1 + \mathrm{erf} \left(\frac{\ln{(r_e)} - \mu}{\sqrt{2}\sigma} \right) \right), \tag{11}$$

where S_h is saturation of gas hydrate (the fraction of pore space occupied by gas hydrate), S_g is the free gas saturation, and S_l is the ice saturation. Solving for effective pore radius as a function of nonwetting phase saturations, the equation is rearranged as follows and incorporated into simulations:

$$r_e = e^{\sqrt{2}\sigma \mathrm{erf}^{-1} \left(1 - 2S_h - 2S_g - 2S_l \right) + \mu}, \tag{12}$$

where r_e is the effective pore radius governing methane solubility of the next pore in which a nonwetting phase can precipitate. This effective pore radius is then used in the Gibbs-Thomson equation to describe

the evolution of the three-phase equilibrium pressure with changing hydrate saturation in the sand layer. This treatment approximates the effect of increasing gas hydrate saturation on methane solubility described in *Rempel* [2011].

In the current work, simulations are performed within the GHSZ and temperatures remain above the freezing temperature of water, so free gas and ice are not stable phases. Therefore, S_g and S_l in equations (11) and (12) are always equal to 0, and capillary interactions between multiple nonwetting phases are not applicable. We apply this process only to sands in the simulation; we ignore pore size distribution effects in the clay layers because gas hydrate is not typically observed in a pore-filling habit in clay sediments in the Terrebonne Basin. Rather, hydrate tends to fill fracture or vein networks in fine-grained, clay-rich sediments, and over a regional scale, gas hydrate saturations as a percentage of clay pore space tend to be small (around 5%) [*Cook et al.*, 2014].

3. Results

Through 1-D simulations, we explore how sand pore size distributions, sand thickness, and burial affect the potential distribution of diffusion-driven methane hydrate accumulations in coarse-grained sands. In 2-D and 3-D, we then demonstrate how hydrate growth patterns can depend on multiple sand layer interactions as well as concentration gradients in multiple dimensions due to sand dip.

We simulate the growth and dissociation of a hydrate-bearing sand layer buried through the GHSZ over geologic time in a Terrebonne Basin-like gas hydrate system, in which a thick, ∼2 km water column and a low geothermal gradient contribute to a thick GHSZ. Methanogenesis properties and environmental parameters used in this work are summarized in Table 1. Although the parameters governing rates of methanogenesis at Walker Ridge are not well constrained, we select values of the reaction rate of methanogenesis, λ, and the organic carbon content at the SMT, α_{SMT}, following *Malinverno* [2010]; the depth of the SMT, z_{SMT}, is estimated based on data at Keathley Canyon [*Kastner et al.*, 2008] and Alaminos Canyon [*Smith and Coffin*, 2014].

In all simulations reported in this study, a binary system of sand and clay lithologies is buried through the GHSZ to a depth of 900 mbsf; sands are characterized in 1-D and 2-D simulations by pore size distributions and in 3-D by a single pore radius, r_{sand}, defining aqueous methane solubility. In all simulations, the clays are described by a single pore radius ($r_{c,max}$ in 1-D and 2-D, and r_{clay} in 3-D), and microbial methanogenesis is only active in the clay lithology.

3.1. One-Dimensional Lagrangian Simulations

One-dimensional simulations were performed in this study to resolve at high vertical resolution the potential hydrate distribution patterns within thin sands buried through the GHSZ.

3.1.1. Pore Size Distribution Effects on Gas Hydrate Growth in Sands

Within a single horizontal sand layer, the distribution of pore sizes can exert significant control on the possible distribution of hydrate throughout the sand. If there is no significant change in solubility within the layer, hydrate forms only at the sand's edges [*Rempel*, 2011]. When incorporating pore size distribution effects, aqueous methane solubility is reformulated additionally as a function of hydrate saturation. Thus, as hydrate forms on the edges of a sand layer, a gradient in solubility within the sand layer itself favors hydrate formation away from the sand's edges (Figure 4).
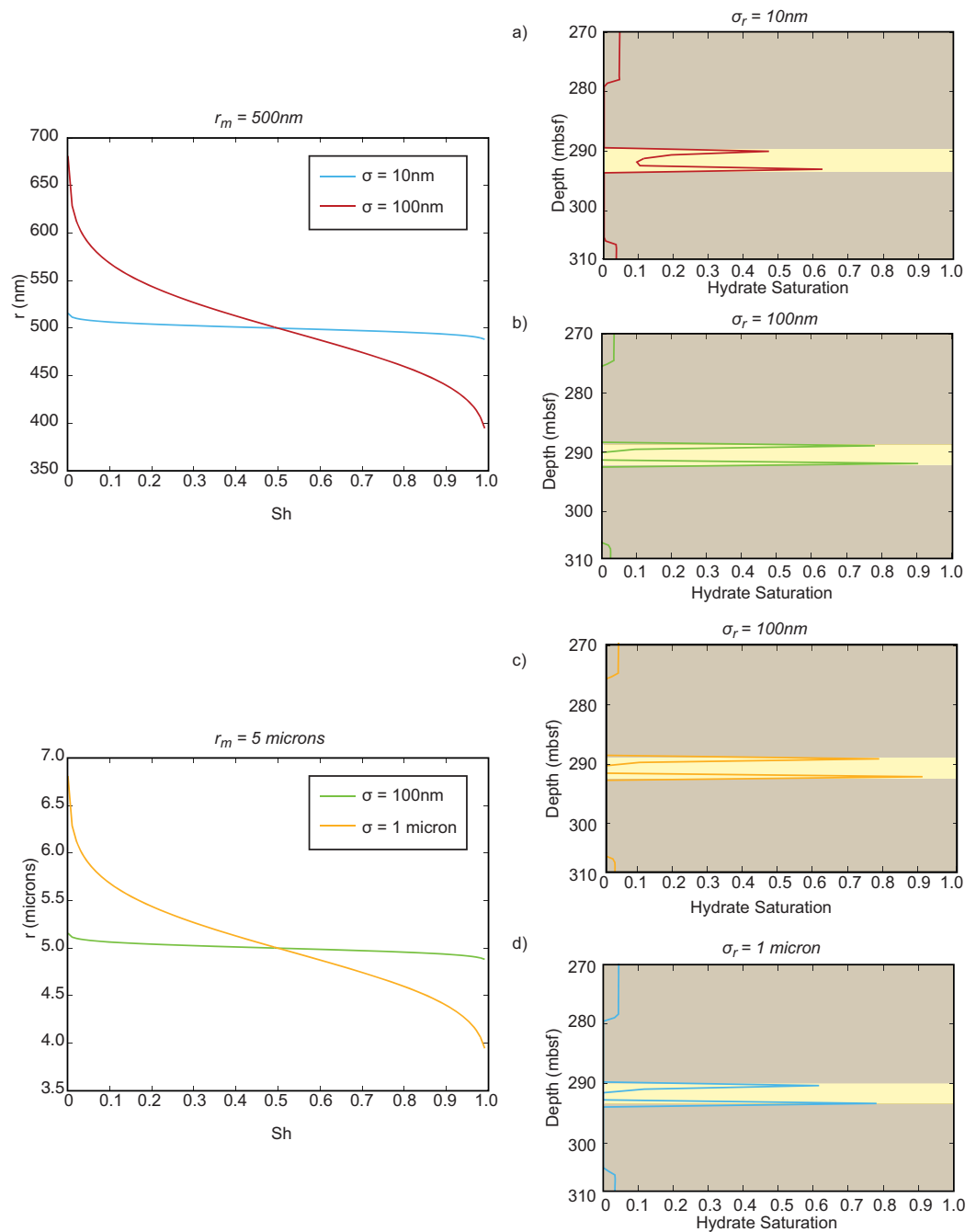
Table 1. Simulation Parameters

Variable Name	1-D and 2-D Lagrangian	3-D Eulerian
Seafloor Depth (m)	1917	1917
Seafloor temperature (°C)	4	4
Geothermal gradient (°C/km)	19	19
BHSZ (m)	900	900
D_s (m²/s)	1×10^{-10}	1×10^{-10}
Dip angle (2-D only) (°)	10	n/a
Gravitational acceleration (m/s²)	9.8	9.8
T_f (K)	273.15	273.15
v_f (mm/yr)	Variable	1
k_α (kg/m³)	2241	2241
λ (s⁻¹)	1×10^{-13}	1×10^{-12}
α_{SMT} (dry wt %)	0.5	0.5
ω (mm/yr)	1.0	1.0
z_{SMT} (m)	10	10
T_{mb} (K)	273.15	273.15
σ_{hl} (N/m)	0.027	0.027
θ (°)	0	0
H_f (kJ/kg)	439	439
ρ_h (kg/m³)	925	925
r_{sand} (μm)	n/a	1
r_{cmax} (μm)	0.2	n/a
r_{clay} (μm)	n/a	0.01
σ_r (μm)	20	n/a
r_m (μm)	20	n/a

Figure 4. (left) Effective pore radius as a function of hydrate saturation, for various pore size distributions. (right) The gas hydrate distribution impact within a thin sand under four pore size distribution scenarios: (a) low median pore size and low standard deviation in pore size; (b) low median pore size and high pore size standard deviation; (c) high median pore size and low standard deviation; (d) high median pore size and high standard deviation.

Since hydrate tends to be present as a fracture-fill in fine-grained sediments, we interpret simulated hydrate saturations in the bounding fine-grained material as fracture filling. If solubility in the fine-grained sediment is lowest in the largest pores, and if no pores can fill with interstitial hydrate, then fracture-filled hydrate growth should be governed by the methane solubility of the largest clay pore. Thus, we define a maximum pore size governing hydrate growth in the clay intervals, $r_{c,max}$.

As is depicted in Figure 4, the distribution of gas hydrate within a thin sand depends heavily on the sand's pore size distribution. If the sand exhibits a low standard deviation in pore size (Figures 4a and 4c), gas

hydrate is unable to accumulate in massive quantities at the center of the sand because the effective aqueous methane solubility is nearly constant within the sand; hydrate growth in a sand characterized by larger pores (Figure 4d) fills with greater amounts of hydrate (nearly 100% of the pore space) at the sand's edges. Contrastingly, in a sand layer characterized by a broad pore size distribution and a relatively low median pore size closer to that of a silty lithology (Figure 4b), hydrate growth toward the center of the sand can reach upward of 20% of the average saturation at the layer's edges. This is not possible, however, in a sand containing entirely large pores (Figure 4d). These results suggest that although a strong sand-clay solubility contrast is required to drive significant diffusive flux of methane from clays to sands, gas hydrate cannot evenly distribute throughout the sand layer unless there exists a significant gradient in aqueous methane solubility within the sand layer itself.

3.1.2. Burial Effects on Gas Hydrate Distribution Patterns in Sands

Since the rate of change in hydrate saturation within a sand grid block depends on the dissolved methane concentration gradient and inversely on grid discretization [*Rempel*, 2011], we impose a lognormal pore size distribution whose median pore size is determined experimentally [*Bihani et al.*, 2015] but whose pore size at 99.7% hydrate saturation is equivalent to $r_{c,max}$. This ensures that as hydrate saturation increases in the sand layer, the gradient in methane concentration between the sand and surrounding clay tends toward zero, imposing a limit on the rate at which hydrate saturations can increase via diffusive methane transport. Figure 5 depicts a schematic of a 1-D simulation alongside simulated hydrate saturations in which one thin sand layer (3.6 m thick) is buried through a microbially active GHSZ at a constant sedimentation velocity, v_{sed} (1 mm/yr in these simulations).

As shown in Figure 5, in a microbially active gas hydrate system with only compaction-driven upward fluid flow, a thin sand layer tends to diffusively soak up methane from surrounding clay material as it is buried. The sand-clay solubility contrast promotes diffusive methane transport to the sand layer; the presence of this discontinuity requires that hydrate-free zones separate a hydrate-bearing sand from hydrate-bearing clay above and below it. Hydrate saturations in the sand layer tend to increase over time while the supply of methane via microbial methanogenesis in the clays outpaces hydrate dissolution due to increasing solubility with burial. Once the input of methane from microbial activity diminishes such that there is net hydrate dissolution in the bounding clays, hydrate growth is still possible in sands until all the hydrate in the surrounding clay material has dissolved.
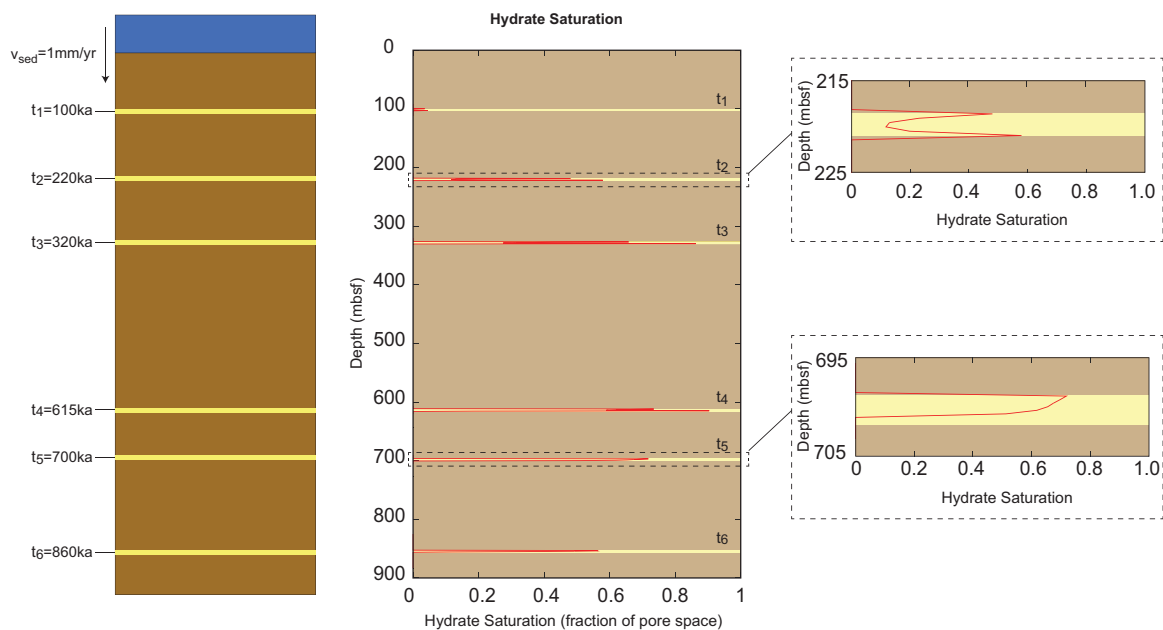

Figure 5. One-dimensional time series evolution of hydrate saturation profiles within a single thin sand layer (3.6 m thick) in a Lagrangian reference frame as it is buried through the hydrate stability zone, incorporating capillary effects on aqueous methane concentration gradients.
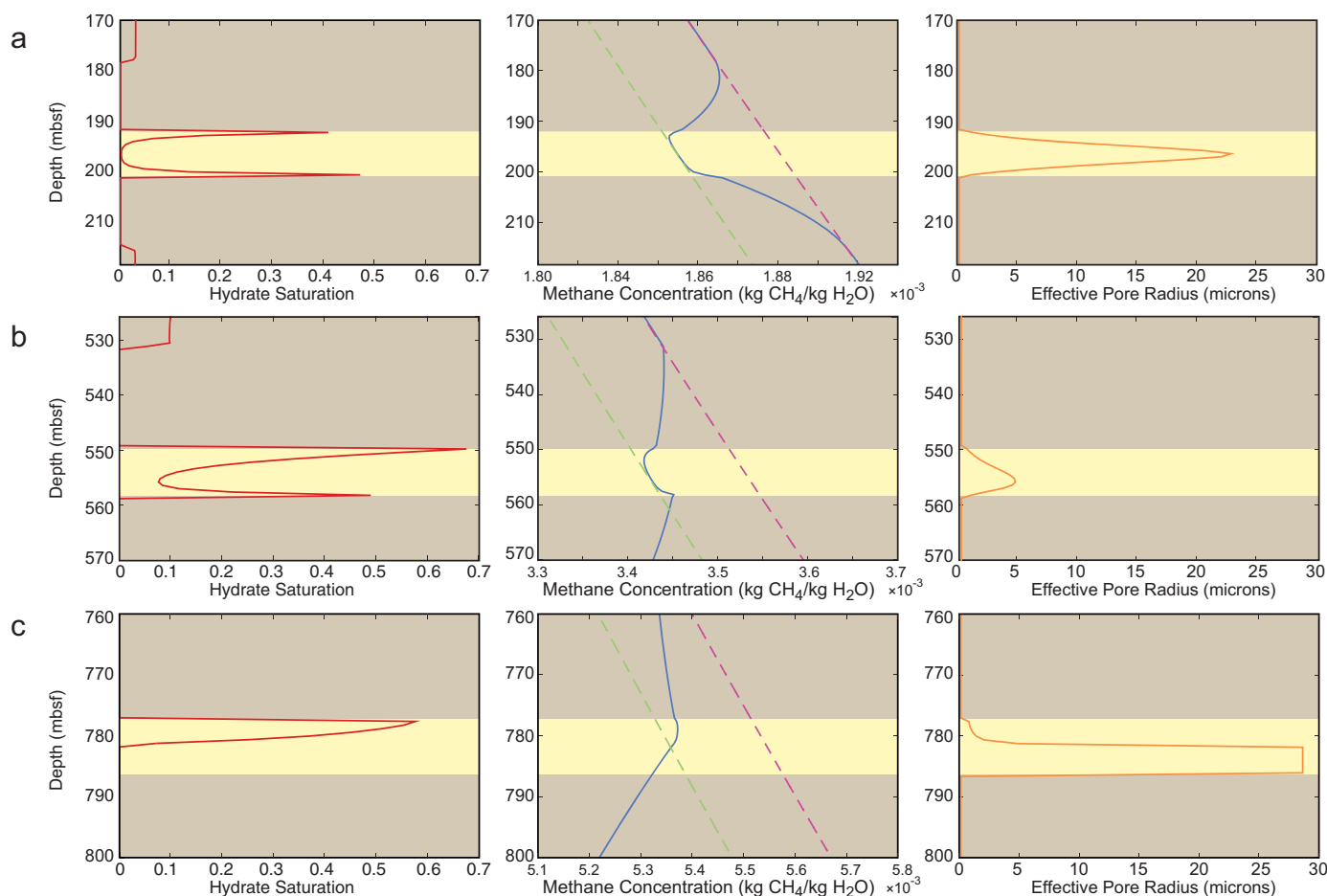
Figure 6. Patterns of gas hydrate distribution (red), dissolved methane concentration (blue), and effective pore radius (orange) governing effective methane solubility within a 6 m thick sand layer as it is buried through the GHSZ (a) early in burial, (b) at an intermediate burial depth, and (c) late in burial. A dashed green line indicates free space bulk aqueous methane solubility, and a dashed magenta line indicates the effective aqueous methane solubility in clay pores. The sand layer is highlighted in yellow, and the bounding clay is highlighted in brown.

Figure 6 highlights three observable trends in gas hydrate growth patterns within a sand layer (6 m thick) as it is buried through the GHSZ. At early time (Figure 6a), hydrate is present in clays above and below the sand layer. The gradient in aqueous methane concentration is fixed by the effective solubility of methane in pore water above and below the hydrate-free zones, and diffusive methane transport is directed entirely toward the sand layer. Hydrate accumulates at a faster rate at the base of the sand than at the top. This is due to a steeper sand-clay solubility gradient at the bottom of the sand (as evidenced by the aqueous methane concentration gradients through the hydrate-free zones) as well as upward advective compaction flux. As hydrate saturations increase at the edges of the sand, the effective sand pore radius decreases and a diffusive gradient within the sand allows for methane transport toward the sand's center.

Once the influx of microbial methane is insufficient to cause further hydrate growth in the clay layer, hydrate contained within the clay beneath the sand layer first begins to dissolve. Because hydrate is still present in the clay, however, an aqueous methane concentration gradient between the bounding clay and the sand layer still exists, so gas hydrate dissolving in the clay layer feeds hydrate that is present in the sand, preserving hydrate in the sand from dissolution with burial.

Once all of the hydrate in the clay beneath the sand layer has dissolved (Figure 6b), hydrate begins to dissolve from the bottom of the sand layer. Although a methane concentration gradient drives diffusive flux out of the base of the sand, a concentration gradient also drives diffusive methane transport from the base of the sand to its center. Net methane migration from above is still directed toward the center of the sand. Hydrate growth can therefore still occur at the top of the sand layer if hydrate still exists in the bounding

clay above the sand (or as long as the methane concentration in this region exceeds the solubility of methane in the pore water of the sand). Once the hydrate within the clay above the sand and at the base of the sand fully dissolves (Figure 6c), hydrate on the upper sand boundary proceeds to dissolve. In this case, the methane concentration gradient drives diffusive methane transport out of the sand from above and below.

It is important to note that the gas hydrate distribution patterns shown here reflect the potential trends in diffusion-driven methane hydrate growth and distribution in sand layers. These patterns depend on how rapidly methane generation decreases with depth and on the initial conditions of the simulation at the time of sand deposition. In the simulations performed here, no methane is initially present at the SMT at the time of deposition of the modeled sand layer. The results of these simulations therefore correspond to the maximum rate at which hydrate dissolution should take place. If methane is present in the system as an initial condition or if the rate of methane generation decreases more slowly with depth than in these simulations, the hydrate distribution pattern illustrated in Figure 6a might be preserved with deeper burial. In certain instances where there is significant methane sourcing at depth in the GHSZ, the system may never exhibit the patterns described in Figures 6b and 6c.

Intriguingly, these simulations illustrate the potential for gas hydrate dissolving within clay over time to feed and preserve the hydrate existing within sand layers against dissolution while burial increases aqueous methane solubility. This suggests that if hydrate deposits are observed to occur in any quantity within clays at depth in close proximity to thin sands, hydrate grown in the sands could have been preserved during burial as the sands soaked up methane from dissolving hydrate in clays.

3.1.3. Sand Layer Thickness Effects on Gas Hydrate Distributions Within a Sand
For a given pore size distribution within a sand layer, the distribution of gas hydrate within a coarse-grained sand layer depends on the sand layer thickness, all else remaining constant. Figure 7 compares the accumulation of gas hydrate within a sand layer at a particular depth for different sand thicknesses, holding constant the grid discretization and the amount of methane generated through microbial methanogenesis in the bounding clays.

For small sand thicknesses (the 3.6 m sand in Figure 7), the aqueous methane concentration gradient between a sand's edge and its center is stronger than that in a thick sand because of the shorter distance over which methane must travel for a given contrast in solubility. The ratio of the minimum to maximum hydrate saturation within a sand (Figure 7) therefore decreases with increasing thickness and eventually reaches 0 at a finite sand thickness. Furthermore, simulations indicate that the average hydrate saturation
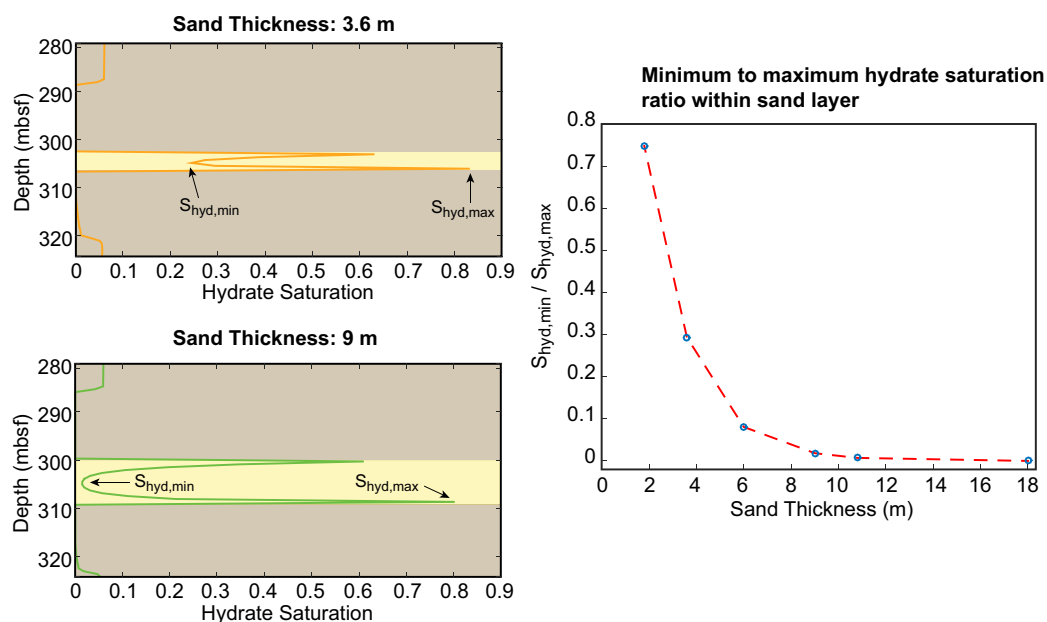

Figure 7. A comparison of minimum to maximum hydrate saturation within a sand for varying thicknesses of sand layers bounded by clays. The sand layer is highlighted in yellow, and the clays are highlighted in brown.
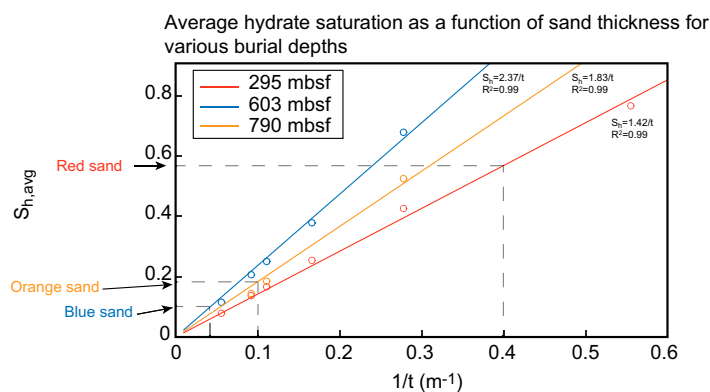
Figure 8. Average hydrate saturation as a function of sand thickness for various burial depths. Open circles represent the results of individual simulations performed in this work for sands of varying thicknesses buried to different depths.

within a coarse-grained sand layer buried through the GHSZ is inversely proportional to the sand's thickness, all else remaining constant (Figure 8). The coefficient of proportionality tends to increase with increasing depth as the sand experiences net hydrate growth, but then at a certain point it begins to decline as hydrate is driven toward net dissolution.

3.1.4. Comparing Simulations to Observations in the Terrebonne Basin

In order to test whether the potential hydrate distribution patterns outlined above can sufficiently explain hydrate accumulations as interpreted from well log data at Walker Ridge in the Terrebonne Basin, we examine the average hydrate saturations contained within modeled sand intervals as a function of sand thickness for different observed depths of sand burial (Figure 8).

Considering the WR313-H hole, dashed gray lines in Figure 8 indicate the approximate depths and thicknesses of the Red, Blue, and Orange sands. One-dimensional modeling results indicate that for a 2.5 m thick Red sand buried to 295 mbsf, the average hydrate saturation in the sand should approach about 60% (Figure 8), if all hydrate were supplied by diffusive migration. This is consistent with the interpretations of *Cook and Malinverno* [2013]. On the other hand, for a 25 m thick Blue sand and a 10.5 m thick Orange sand, simulation results indicate that diffusion alone can produce about 10% and 20% average hydrate saturations in each interval, respectively. This is significantly less hydrate than is actually observed in these intervals (an average of about 60% in the Blue sand and 65% in the Orange sand).

The results of these models indicate that (1) diffusion is likely not the only methane migration mechanism at play in the thick sands buried deep in the GHSZ in the Terrebonne Basin; (2) heterogeneities within sand layers could be enhancing diffusive methane flux to coarse-grained intervals; and/or (3) microbial methanogenesis cannot be represented as simplistically as in this study. The thickness, depth, and significance of hydrate accumulation in the Blue sand suggest that methane hydrate accumulation in this interval is likely predominantly driven by fluid advection. Additionally, the Blue sand is characterized by significant fine-grained interbedding between hydrate accumulations in coarse-grained intervals. Methane solubility gradients between thin laminations could enhance methane transport within the sand unit and thus bolster hydrate growth in the unit's coarser-grained sections. Such fine-scale heterogeneities are not currently captured but are the subject of future work. The Orange sand, occurring deeper than the Blue sand, is made up of much less interbedding. It is likely that advective transport due to long-range gas transport and/or overpressuring is enhancing hydrate accumulations in this unit.

3.2. Two-Dimensional Lagrangian Simulations of a Dipping Sand Layer

Two-dimensional simulations performed in this study demonstrate the potential hydrate accumulation patterns in the vicinity of a dipping sand layer in the presence of aqueous methane concentration gradients in two dimensions as opposed to just one dimension.

During earlier stages of burial (Figure 9a), when methane input due to microbial methanogenesis outpaces the increase in methane solubility of the system with burial, gas hydrate growth proceeds in both the sand layer and the bounding clay, but a hydrate-free zone separates hydrate accumulations in both sections. Everywhere in the system, dissolved methane concentrations increase downdip (Figure 9). However, perpendicular to the sand layer, dissolved methane concentrations decrease as they approach the sand (due to
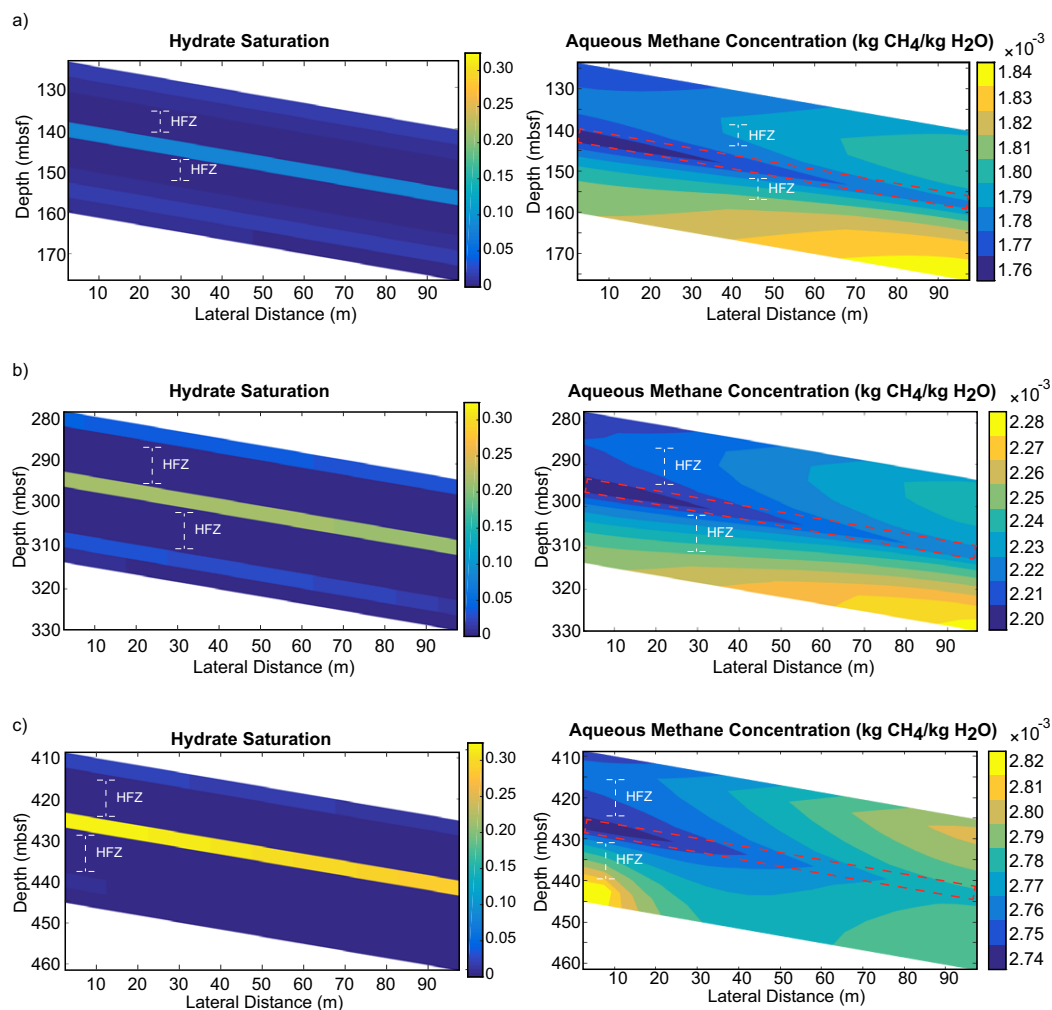
Figure 9. Simulated hydrate saturations, separated by hydrate-free zones (HFZ), and dissolved methane concentrations in a dipping, 3.6 m thick sand layer as it is buried through the hydrate stability zone (a) early in burial, (b) at an intermediate burial depth, and (c) later in burial.

sand-clay variations in solubility), resulting in net methane transport toward the sand from above and below.

As the system is buried, the sand-clay solubility difference at the downdip end of the sand increases at a faster rate than updip because the rate of change in solubility increases with increasing depth [*Xu and Ruppel*, 1999]. In combination with a decreasing methane input due to methanogenesis and an upward fluid compaction flux relative to the sediment grains, this effect causes hydrate to dissolve in the clay downdip and beneath the sand faster than updip and above the sand. Dissolution occurs in the clay both above and below the sand layer, but the sand layer is shielded from dissolution while hydrate exists in the nearby clay because the gradient in methane concentration within the hydrate-free zones always directs methane transport toward the sand (Figure 9b). As is illustrated in Figure 9c, hydrate dissolves fully first downdip and beneath the sand. A region of high methane concentration still exists updip where the clay layer contains hydrate. Since hydrate is absent in some of the clay downdip beneath the sand, hydrate growth in the sand slows downdip in comparison to updip.

At all stages of the 2-D simulations, hydrate saturations appear lower than those predicted in 1-D simulations. In 2-D, a 3.6 m thick sand layer buried to 295 mbsf accumulates an average hydrate saturation of 23%. One-dimensional modeling suggests (Figure 8) that the average hydrate saturation in this sand should equal 1.42/3.6, or about 39% hydrate saturation. The discrepancy between 1-D and 2-D models could be due to the fact that 2-D simulations can capture the aqueous methane concentration gradient in two
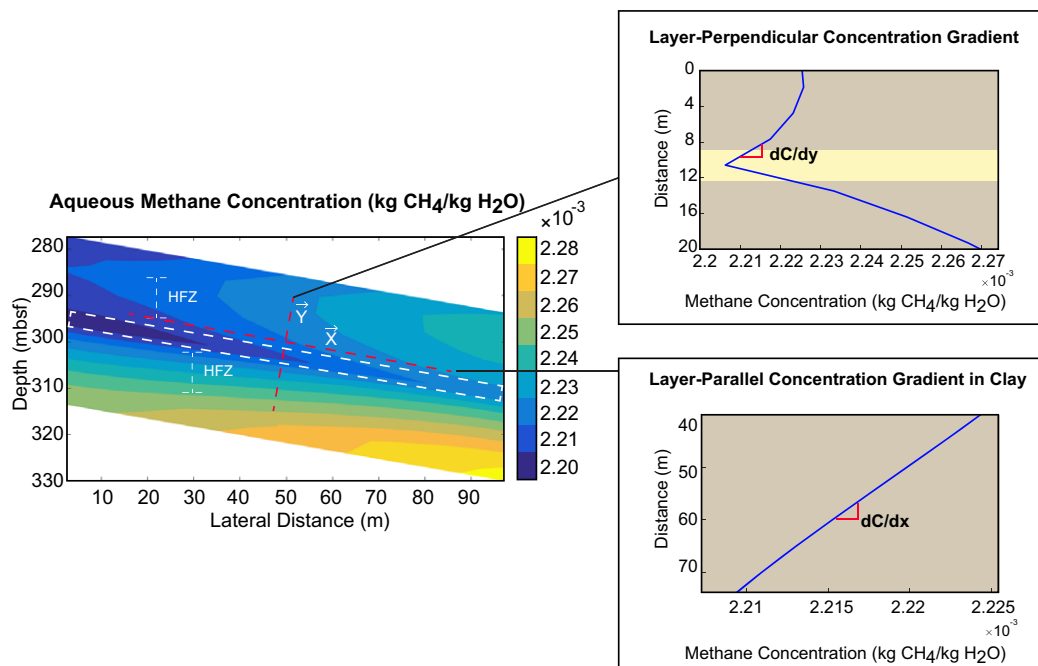
Figure 10. Methane concentration profiles (indicated by red dashed lines) are drawn parallel and perpendicular to the dipping sand layer (outlined by a white dashed line) shown in Figure 9b.

dimensions as opposed to just one. In 1-D models, the aqueous methane concentration gradient is always oriented perpendicular to the sand. In 2-D, however, there can be a component of the concentration gradient parallel to the sand layer.

As an example, Figure 10 illustrates the components of the methane concentration gradients perpendicular to the sand and parallel to the sand within the nearby clay. When the sand layer is buried to 295 mbsf, the layer-perpendicular concentration gradient between the sand layer and clay immediately above is approximately 2.5×10^{-6} kg CH_4/kg H_2O/m. Contrastingly, the layer-parallel methane concentration gradient is about 20% of this value (5×10^{-7} kg CH_4/kg H_2O/m). In 1-D, the methane concentration gradient (necessarily perpendicular to the sand) is approximately 1.2×10^{-5} kg CH_4/kg H_2O/m when the sand layer is buried to the same depth, which is about 5 times greater than the layer-perpendicular methane concentration gradient in 2-D. For the same amount of methane available per unit volume, the presence of a layer-parallel component to the methane concentration gradient ultimately leads to less diffusive methane transport to dipping sand grid blocks in 2-D as compared to 1-D.

Although these 2-D simulations are helpful for better understanding the multidimensional nature of aqueous methane concentration gradients in diffusion-dominated systems, the sand modeled here spans only about 10 m in depth. This model therefore does not adequately demonstrate the potential differences in hydrate distributions along the dip of a sand body spanning greater depths; for this we instead look to 3-D simulations.

3.3. Basin-Scale 3-D Simulations

We employed 3-D basin-scale modeling to better understand how, on a regional scale, gas hydrate distributions in diffusion-dominated systems could be influenced by basin geometry. By directly incorporating the results of 3-D seismic interpretation, hydrate growth is tracked in four distinct sand layers as they are buried and rotated through the hydrate stability zone in a fixed reference frame. Sand layers imported in these simulations extend about 30 km^2 down through the hydrate stability zone and exhibit dip as well as curvature. Three-dimensional modeling is therefore able to demonstrate spatial variation of gas hydrate saturations in sand layers in a way that is not possible in 1-D and 2-D. Additionally, a further benefit of modeling in 3-D is that it can capture the interaction potential between multiple dipping sands whose orientation to one another changes in space and time.
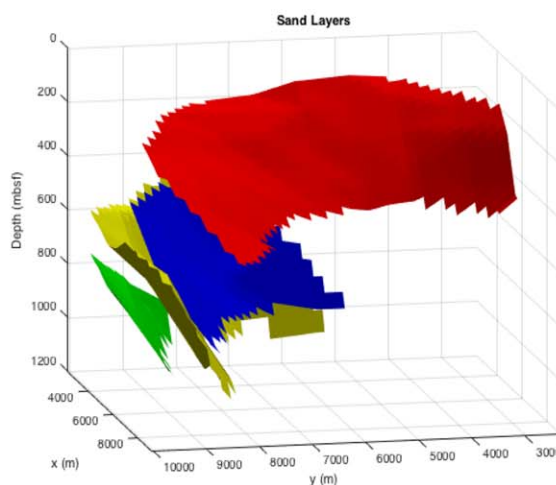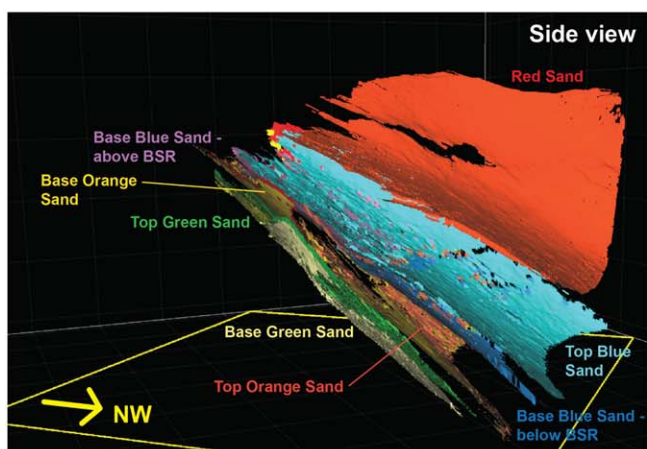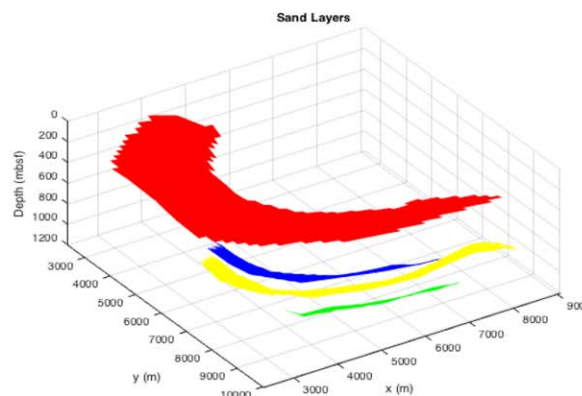
Interpreted Seismic Data
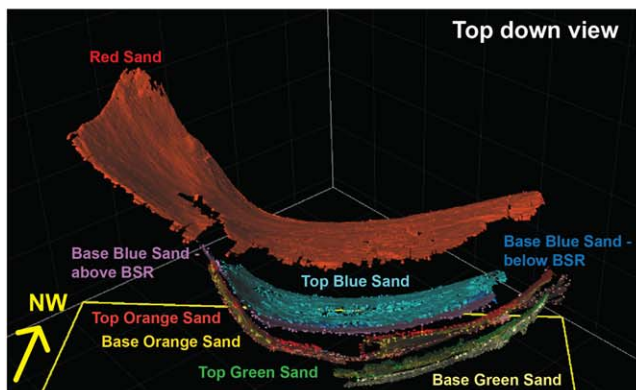
Simulation

Figure 11. Three-dimensional perspective of interpreted sand horizons, which are imported into the simulator. Data for image courtesy of WesternGeco.

The results of 3-D seismic interpretation of sand layer geometry in the Terrebonne Basin are incorporated into 3-D simulations to produce synthetic hydrate saturation profiles using realistic stratigraphic relationships between sands. Horizons interpreted from seismic data, which delineate the top and bottom surface of sand layers, are imported directly into the simulator and mapped from the geographic coordinate system to grid blocks in the simulation environment (Figure 11).

As depicted in Figure 12, full-scale 3-D modeling yields similar hydrate growth patterns to those seen in 1-D and 2-D models: hydrate saturations in deeply buried sands increase with depth, but at a certain depth of burial, hydrate begins to dissolve. Just as in 1-D and 2-D, the depth and rate at which dissolution occurs depends on the initial conditions imposed in the simulation; the results shown here present a representative set of potential hydrate formation and dissolution characteristics for a diffusion-dominated system.

In 3-D simulations, hydrate accumulates in higher saturations downdip because the sand-clay solubility contrast is larger at depth. Although the sand layers comprising methane hydrate reservoirs of interest to this study are nearly planar, they do exhibit some curvature, tend to converge toward each other, and thin out in the updip direction. There is a noticeable absence of significant hydrate accumulation in the topmost sand layer near where it is closest to the sand layer beneath it. The close proximity of the two sand layers could create competition for diffusion of methane from the clay between them; if the clay layer between the two sands were not thick enough, neither of the sand layers would be able to soak up methane to their maximum potential. This finding suggests that while planar geometries may yield close approximations of hydrate distributions on a regional scale, using 2-D cross sections to model multilayered hydrate systems
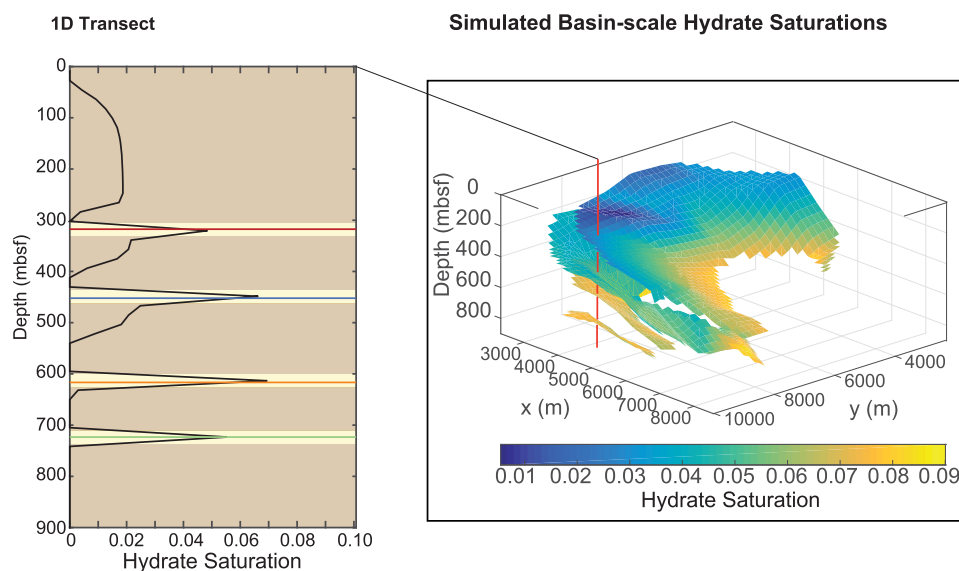
Figure 12. Three-dimensional simulated gas hydrate saturations in four sand layers (18.3 m thick), accompanied by a 1-D transect. In the 1-D transect, sand layers are highlighted in yellow, and clays are highlighted in brown.

could overestimate hydrate saturations if sand layers converge out of plane. This may represent a significant source of error in modeling systems like the salt-withdrawal basins of the northern Gulf of Mexico.

Comparing regional trends to a 1-D transect (Figure 12), it is easier to see how, deep in the sediment column, an increase in methane solubility with burial begins to dissolve gas hydrate present in sand layers (as was seen in prior 1-D and 2-D simulations). During burial, while hydrate still exists in clays surrounding the sands, the sand layers still experience net hydrate growth. When hydrate in the clay layers completely dissolves due to increasing methane solubility with burial, hydrate in the sands then begins to dissolve. This confirms the effect seen in 1-D and 2-D simulations on a regional scale and further implies that hydrate-filled clay intervals could be associated with preserved hydrate accumulations in nearby hydraulically connected sands. Preservation of high hydrate saturations at depth may require an additional advective component of methane supply in the absence of hydrate-bearing clay nearby.

The drawbacks to lower resolution simulations include an inability to resolve hydrate-free zones between sand layers because the sand-clay methane concentration gradient can span a shorter distance than is resolved between two grid blocks. Diffusive methane transport from clay grid blocks bordering sands acts over a longer distance and therefore reaches sands more slowly than in a higher-resolution simulation for the same sand-clay solubility contrast. This is particularly problematic when a sand layer is moving through the simulation domain with a certain sedimentation velocity. Therefore, to make 3-D simulations at lower resolution comparable to 1-D and 2-D simulations, our goal was to achieve similar trends in hydrate accumulation between all simulations. To achieve consistency in 3-D with 1-D and 2-D models, in 3-D the sand-clay pore size contrast was enhanced and the reaction rate of microbial methanogenesis was increased. An increase in the sand-clay pore size contrast enhances the sand-clay solubility difference; if enough methane is present, this increases the sand-clay methane concentration difference, which works to drive methane faster across a coarser grid block spacing. To provide this enhancement in the concentration, methane must be supplied faster, and the microbial methanogenesis reaction rate must be increased. The total mass of organic carbon per unit volume available to each system is maintained consistent across 1-D, 2-D, and 3-D simulations.

To first approximation, agreement among 1-D, 2-D, and 3-D simulations is verified by observing generally increasing sand hydrate saturations to about 600 mbsf, at which point hydrate accumulations in bounding clays become diminished and dissolution proceeds in sand layers. Additionally, we compare the cumulative mass transport to the sand layers by scaling hydrate saturations by grid discretization. At about 320 mbsf, 3-D simulations yield a hydrate saturation of 4.8% in an 18.3 m thick sand; if the same mass were to be contained in a 3.6 m thick sand, hydrate saturation would be 24%. In simulations involving a 3.6 m thick sand,

the average hydrate saturation in the sand is 39% in 1-D and 23% in 2-D. The consistency between 2-D and 3-D simulations is likely due to their ability to capture diffusive methane transport along concentration gradients in multiple dimensions, while in 1-D all methane transport occurs perpendicular to the sand layer.

4. Conclusions

This study establishes the potential methane hydrate distribution patterns that can form due to diffusion in coarse-grained sediments buried through the GHSZ from the scale of a single sand layer up to an entire basin. One-dimensional simulations performed in this study illustrate that in marine environments in which microbial methanogenesis generates dissolved methane in clay sediments, diffusive action can generate large hydrate saturations in relatively thin sands buried at shallow depths in the GHSZ, such as the Red sand at WR313-H. Comparing simulations to log data at the Terrebonne Basin, although we do not incorporate lithologic heterogeneities within thick sand layers, we show that diffusion is not necessarily effective in generating large hydrate saturations in thick, homogeneous sand layers buried deeply within the GHSZ. This is because the amount of methane transported by diffusion from adjacent fine-grained sediments is distributed over a relatively large sand bed thickness. Also, the increase in methane solubility with depth can lead to dissolution of hydrate in these layers; the extent of dissolution in our simulations depends on the intensity of microbial methane generation at depth and on the assumed initial conditions of the simulation.

We find through high-resolution 1-D simulations that gas hydrate in diffusion-dominated systems tends to concentrate at the edges of sand layers. To generate hydrate in a sand's center through diffusive transport, effective aqueous methane solubility must be enhanced at the sand's edges. Although we model this effect as dependent on sediment pore size distributions, pore curvature alteration with hydrate growth or changes in the aqueous methane diffusion coefficient with changing pore tortuosity should also lead to similar effects. As the sands are buried by sedimentation, high hydrate saturations in sands can be preserved if bounding clays contain hydrate or at least contain methane in concentrations above the solubility of the sand layer. If these conditions are not met, it is likely that high hydrate saturations in sand intervals are the result of advection being the dominant methane transport mechanism.

Two-dimensional simulations demonstrate that in a dipping sand layer in a diffusion-dominated environment, hydrate tends to accumulate along the sand's dip and is separated from hydrate-filled clays by hydrate-free zones above and below. Over time, methane solubility downdip increases faster than updip, so hydrate in the clay intervals tends to dissolve faster downdip and below the sand. Additionally, when methane concentrations at depth are insufficient to generate hydrate within a particular sediment volume, compaction-driven fluid transport can work to dissolve hydrate downdip and beneath a sand layer. This can lead to the asymmetric hydrate distributions observed along a sand layer in 2-D simulations as well as within a sand layer in 1-D. Concentration gradients exist parallel and perpendicular to the sand, so less methane is transported to the sands overall in 2-D and 3-D simulations as compared to 1-D. In 3-D, simulations clearly illustrate that at a regional scale, hydrate saturations tend to increase downdip until the supply of methane from surrounding fine-grained material cannot fuel further hydrate growth. While 3-D simulations confirm the observation in 1-D that hydrate in clays can preserve high hydrate saturations in sand through burial, they also demonstrate that convergence of sand layers in multilayered systems can lead to anomalous reductions in hydrate saturation due to competitive diffusion.

Other potentially important drivers of hydrate growth in thin sand layers buried within a diffusion-dominated gas hydrate system include gradients in lithology between clays and sands, time-varying rates of microbial methanogenesis, and changes in the pore water methane diffusion coefficient with variable hydrate saturation. Our simulations indicate that sand with small median pore sizes and broad pore size distributions can push hydrate growth toward the center of a sand layer. In future work we will incorporate a gradient in lithology between clay and sand instead of describing our system as simply containing either sand or clay lithologies; we should similarly see enhanced methane transport from the edges of sands toward their center. Furthermore, incorporating a time-dependent rate of microbial methanogenesis may more accurately represent different depositional environments with different concentrations of organic carbon and methanogens of varying metabolism. Finally, because increased pore-filling hydrate saturations make pore space more tortuous, the diffusion coefficient of methane in water decreases with increasing

hydrate saturation. Incorporating this effect into simulations would slow the process of diffusion with increasing hydrate saturation, thus potentially diminishing the total amount of gas hydrate that can accumulate at the edges of a sand layer.

References

Anderson, R., B. Tohidi, and J. B. W. Webber (2009), Gas hydrate growth and dissociation in narrow pore networks: Capillary inhibition and hysteresis phenomena, *Geol. Soc. Spec. Publ.*, *319*(1), 145–159.

Berner, R. A. (1980), *Early Diagenesis: A Theoretical Approach*, Princeton Univ. Press, Princeton, N. J.

Bhatnagar, G., W. G. Chapman, G. R. Dickens, B. Dugan, and G. J. Hirasaki (2007), Generalization of gas hydrate distribution and saturation in marine sediments by scaling of thermodynamic and transport processes, *Am. J. Sci.*, *307*(6), 861–900.

Bihani, A., H. Daigle, A. Cook, D. Glosser, and A. Shushtarian (2015), Pore size distribution and methane equilibrium conditions at Walker Ridge Block 313, northern Gulf of Mexico, Abstract OS23B-1999 presented at 2015 Fall Meeting, AGU, San Francisco, Calif, 15 Dec.

Boswell, R., M. Frye, D. Shelander, W. Shedd, D. R. McConnell, and A. Cook (2012), Architecture of gas-hydrate-bearing sands from Walker Ridge 313, Green canyon 955, and Alaminos canyon 21: Northern deepwater Gulf of Mexico, *Mar. Pet. Geol.*, *34*(1), 134–149.

Buffett, B. A. (2000), Clathrate hydrates, *Annu. Rev. Earth Planet. Sci.*, *28*, 477–507.

Chatterjee, S., G. Bhatnagar, B. Dugan, G. R. Dickens, W. G. Chapman, and G. J. Hirasaki (2014), The impact of lithologic heterogeneity and focused fluid flow upon gas hydrate distribution in marine sediments, *J. Geophys. Res. Solid Earth*, *119*, 6705–6732, doi:10.1002/2014JB011236.[10.1002/2014JB011236]

Claypool, G. E., and I. R. Kaplan (1974), The origin and distribution of methane in marine sediments, in *Natural Gases in Marine Sediments*, edited by I. R. Kaplan, pp. 99–139, Plenum, New York.

Clennell, M. B., M. Hovland, J. S. Booth, P. Henry, and W. J. Winters (1999), Formation of natural gas hydrates in marine sediments: 1. Conceptual model of gas hydrate growth conditioned by host sediment properties, *J. Geophys. Res.*, *104*, 22,985–23,003.

Collett, T. S. (2002), Energy resource potential of natural gas hydrates, *AAPG Bull.*, *86*, 1971–1992.

Collett, T. S., M. W. Lee, M. V. Zyrianova, S. A. Mrozewski, G. Guerin, A. E. Cook, and D. S. Goldberg (2012), Gulf of Mexico gas hydrate joint industry project leg II logging-while-drilling data acquisition and analysis, *Mar. Pet. Geol.*, *34*(1), 41–61.

Cook, A. E., and A. Malinverno (2013), Short migration of methane into a gas hydrate-bearing sand layer at Walker Ridge, Gulf of Mexico, *Geochem. Geophys. Geosyst.*, *14*, 283–291, doi:10.1002/ggge.20040.

Cook, A. E., D. Goldberg, and R. L. Kleinberg (2008), Fracture-controlled gas hydrate systems in the northern Gulf of Mexico, *Mar. Pet. Geol.*, *25*(9), 932–941.

Cook, A. E., D. Goldberg, and A. Malinverno (2014), Natural gas hydrates occupying fractures: A focus on non-vent sites on the Indian continental margin and the northern Gulf of Mexico, *Mar. Pet. Geol.*, *58*, 278–291, doi:10.1016/j.marpetgeo.2014.04.013.

Daigle, H., and B. Dugan (2010), Origin and evolution of fracture-hosted methane hydrate deposits, *J. Geophys. Res.*, *115*, B11103, doi:10.1029/2010JB007492.

Daigle, H., and B. Dugan (2011), Capillary controls on methane hydrate distribution and fracturing in advective systems, *Geochem. Geophys. Geosyst.*, *12*, Q01003, doi:10.1029/2010GC003392.

Daigle, H., A. Cook, and A. Malinverno (2015), Permeability and porosity of hydrate-bearing sediments in the northern Gulf of Mexico, *Mar. Pet. Geol.*, *68*, 551–564.

Davie, M. K., and B. A. Buffett (2001), A numerical model for the formation of gas hydrate below the seafloor, *J. Geophys. Res.*, *106*, 497–514.

Davie, M. K., and B. A. Buffett (2003), Sources of methane for marine gas hydrate: Inferences from a comparison of observations and numerical models, *Earth Planet. Sci. Lett.*, *206*, 51–63.

Dickens, G. R., J. R. O'Neil, D. K. Rea, and R. M. Owen (1995), Dissociation of oceanic methane hydrate as a cause of the carbon isotope excursion at the end of the Paleocene, *Paleoceanography*, *10*, 965–971.

Frederick, J. M., and B. A. Buffett (2011), Topography-and fracture-driven fluid focusing in layered ocean sediments, *Geophys. Res. Lett.*, *38*, L08614, doi:10.1029/2010GL046027.

Frye, M. (2008), Preliminary evaluation of in-place gas hydrate resources, *MMS Rep. 2008-004*, 136 pp., Min. Manage. Serv., U.S. Dep. of the Inter., Washington, D. C.

Frye, M., W. Shedd, and R. Boswell (2012), Gas hydrate resource potential in the Terrebonne Basin, Northern Gulf of Mexico, *Mar. Pet. Geol.*, *34*(1), 150–168.

Garg, S. K., J. W. Pritchett, A. Katoh, K. Baba, and T. Fujii (2008), A mathematical model for the formation and dissociation of methane hydrates in the marine environment, *J. Geophys. Res.*, *113*, B01201, doi:10.1029/2006JB004768.

Haines, S. S., P. Hart, W. W. Shedd, and M. Frye (2014), Seismic investigation of gas hydrates in the gulf of Mexico: 2013 multi-component and high-resolution 2D acquisition at GC955 and WR313, Paper OTC-25318-MS, in *Proceedings of the Offshore Technology Conference held in Houston*, 18 pp.

Haynes, W. M., and D. R. Lide (2010), Handbook of chemistry and physics, in *National Institute for Standards and Technology*, CRC Press, New York, N. Y.

Hedges, J. I., and R. G. Keil (1995), Sedimentary organic matter preservation: An assessment and speculative synthesis, *Mar. Chem.*, *49*, 81–115.

Henry, P., M. Thomas, and M. B. Clennell (1999), Formation of natural gas hydrates in marine sediments: 2. Thermodynamic calculations of stability conditions in porous sediments, *J. Geophys. Res.*, *104*, 23,005–23,022.

Kastner, M., G. Claypool, and G. Robertson (2008), Geochemical constraints on the origin of the pore fluids and gas hydrate distribution at Atwater Valley and Keathley Canyon, northern Gulf of Mexico, *Mar. Pet. Geol.*, *25*(9), 860–872.

Koh, C. A., R. E. Westacott, W. Zhang, K. Hirachand, J. L. Creek, and A. K. Soper (2002), Mechanisms of gas hydrate formation and inhibition, *Fluid Phase Equilibria*, *194*, 143–151.

Kvenvolden, K. A. (1998), A primer on the geological occurrence of gas hydrate, *Geol. Soc. London Spec. Publ.*, *137*(1), 9–30.

Lide, D. R. (ed.) (2004), *Handbook of Chemistry and Physics*, vol. 85, CRC Press.

Liu, X., and P. B. Flemings (2011), Capillary effects on hydrate stability in marine sediments, *J. Geophys. Res.*, *116*, B07102, doi:10.1029/2010JB008143.

Malinverno, A. (2010), Marine gas hydrates in thin sand layers that soak up microbial methane, *Earth Planet. Sci. Lett.*, *292*, 399–408.

Malinverno, A., and D. S. Goldberg (2015), Testing short-range migration of microbial methane as a hydrate formation mechanism: Results from Andaman Sea and Kumano Basin drill sites and global implications, *Earth Planet. Sci. Lett.*, *422*, 105–114.

Mienert, J., M. Vanneste, S. Bünz, K. Andreassen, H. Haflidason, and H. P. Sejrup (2005), Ocean warming and gas hydrate stability on the mid-Norwegian margin at the Storegga Slide, Mar. *Pet. Geol.*, *22*(1), 233–244.

Milkov, A. V., R. Sassen, I. Novikova, and E. Mikhailov (2000), Gas hydrates at minimum stability water depths in the Gulf of Mexico: Significance to geohazard assessment, *Trans. Gulf Coast Assoc. Geol. Soc.*, *50*, 217–224.

Moridis, G. J. (2003), Numerical studies of gas production from methane hydrates, *SPE J.*, *8*(4), 359–370.

Nole, M., H. Daigle, A. E. Cook, and A. Malinverno (2016), Short-range, overpressure-driven methane migration in coarse-grained gas hydrate reservoirs, *Geophys. Res. Lett.*, *43*, 9500–9508, doi:10.1002/2016GL070096.

Paull, C. K., and W. P. Dillon (2001), *Natural Gas Hydrates: Occurrence, Distribution, and Detection*, Geophys. Monogr. Ser., vol. 124, AGU, Washington, D. C.

Pohlman, J. W., M. Kaneko, V. B. Heuer, R. B. Coffin, and M. Whiticar (2009), Methane sources and production in the northern Cascadia margin gas hydrate system, *Earth Planet. Sci. Lett.*, *287*(3), 504–512.

Rempel, A. W. (2011), A model for the diffusive growth of hydrate saturation anomalies in layered sediments, *J. Geophys. Res.*, *116*, B10105, doi:10.1029/2011JB008484.

Sloan, E. D., and C. A. Koh (2007), *Clathrate Hydrates of Natural Gases*, 3rd ed., 721 pp., CRC Press, Boca Raton, Fla.

Smith, J. P., and R. B. Coffin (2014), Methane flux and authigenic carbonate in shallow sediments overlying methane hydrate bearing strata in Alaminos Canyon, Gulf of Mexico, *Energies*, *7*, 6118–6141, doi:10.3390/en7096118.

Sun, X., and K. K. Mohanty (2006), Kinetic simulation of methane hydrate formation and dissociation in porous media, *Chem. Eng. Sci.*, *61*(11), 3476–3495.

Waseda, A. (1998), Organic carbon content, bacterial methanogenesis, and accumulation processes of gas hydrates in marine sediments, *Geochem. J.*, *32*(3), 143–157.

Xu, W., and C. Ruppel (1999), Predicting the occurrence, distribution, and evolution of methane gas hydrate in porous marine sediments, *J. Geophys. Res.*, *104*, 5081–5095.